Inorganic Chemistry

pubs.acs.org/IC

Article

Insight into the Growth Mechanism and Photocatalytic Behavior of Tubular Hierarchical ZnO Structures: An Integrated Experimental and Theoretical Approach

Ankica Šarić,* Martina Vrankić, Dirk Lützenkirchen-Hecht, Ines Despotović, Željka Petrović, Goran Dražić, and Franz Eckelt

Cite This: *Inorg. Chem.* 2022, 61, 2962−2979

Read Online

ACCESS | Metrics & More | Article Recommendations | Supporting Information

ABSTRACT: The hydrothermal synthesis of zinc oxide (ZnO) particles from zinc acetylacetonate monohydrate in "pure" aqueous solution and in aqueous NaOH solution at 90 °C is reported. The structural and morphological properties of ZnO particles were investigated by powder X-ray diffraction, X-ray absorption spectroscopy (XAS), field emission scanning electron microscopy, and transmission electron microscopy. The effect of NaOH on the growth mechanism and photocatalytic performance of hierarchical ZnO structures was investigated. The experimental findings, supported by results of quantum chemical calculations at the level of density functional theory, were used to propose the mechanism of nucleation and preferential growth of finely tuned hollow and nonhollow ZnO structures and their effects on the photocatalytic activity. The calculations indicate that the process of ZnO nucleation in "pure" aqueous solution mainly proceeds by the reaction of small monomers, while tetramers play a crucial role in aqueous NaOH solution. Both the preferred ZnO nanostructure and microstructure growth processes are driven by O−H···O hydrogen bonds as controlling elements. The calculated values of the $E_{O\cdots H}$ interaction indicate a stronger interaction via O−H···O hydrogen bonds in "pure" aqueous media ($E_{O\cdots H} = -11.73$ kcal mol^{-1}) compared to those obtained in aqueous NaOH solution ($E_{O\cdots H} = -8.41$ kcal mol^{-1}). The specific structural motif of the $(ZnO{-}H_2O)_{12}$ dodecamers with calculated negative ΔG^*_{INT} free release energy indicates that the formation of anisotropic nanocrystalline ZnO with the *c*-axis as the primary growth direction is spontaneous and accelerated exclusively in "pure" aqueous solution, whereas it is an unfavorable endergonic process in aqueous NaOH solution ($\Delta G^*_{INT} > 0$). Efforts have been made to determine the photocatalytic efficiency of the ZnO samples based on the XAS measurements. ZnO particles obtained in "pure" aqueous solution show the highest photocatalytic activity due to the presence of a larger amount of oxygen vacancies.

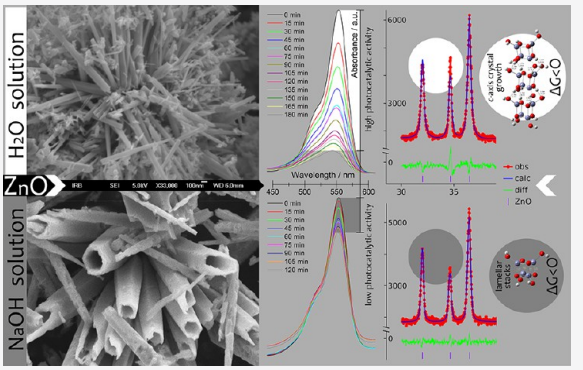

INTRODUCTION

Zinc oxide is one of the most important and widely used metal oxides with applications in very diverse fields ranging from catalysis to electronics, energy harvesting, cosmetics, and biomedicine. The high chemical stability and photostability are useful prerequisites for the use of ZnO as a photocatalyst.[1,2] ZnO is a much better conductor of electrons and holes than many other semiconducting photocatalysts with the advantage that the catalyzed reaction can be carried out in an almost neutral solution.[3] For these reasons, as well as its similar bandgap to TiO_2 and lower toxicity, ZnO is the gold standard in photocatalytic wastewater treatment as a replacement for TiO_2.[4] Some researchers[5,6] reported that the photocatalytic efficiency of ZnO nanocrystals mainly depends on the type and concentration of oxygen defect. Due to the advantages of the photocatalytic process, a review paper[7] was recently published on the selection of suitable methods for the preparation of photocatalysts to obtain the desired size of ZnO nanostructures, which were attempted to improve their photoreaction. Undoubtedly, ZnO has aroused worldwide research interest due to its low toxicity, biocompatibility, and a variety of morphologies.[8−11] Morphologically diverse ZnO nanostructures allow a wide area of application due to the fact that the behavior of ZnO is related to their morphology. Wiesmann et al.[11] reported a significant role of ZnO nanoparticles (NPs) as innovative agents for medical applications for therapeutic purposes in cancer medicine.

Received: December 15, 2021
Published: February 1, 2022

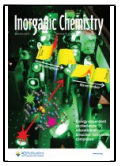

https://doi.org/10.1021/acs.inorgchem.1c03905
Inorg. Chem. 2022, 61, 2962−2979

Among the various synthesis methods, solution-based approaches are advantageous as they provide an excellent controllability of the growth mechanism of ZnO structures. ZnO also serves as a biocompatible, antibacterial, and antiviral agent, which enables its use in biomedical applications.[12,13] Inspired by their proven curative effects on herpes simplex and influenza viruses,[13] ZnO NPs were subjected to various in vitro characterizations and cellular uptake studies in human lung fibroblast cells.[14] The mechanism of ZnO NPs against COVID-19 targets via hydrogen bond formation has been reported in an article published in 2021.[14] The reactivity of ZnO in most applications is due to its interaction with an aqueous solvent. There are few studies on the molecular and dissociative adsorption of H_2O on ZnO surfaces.[15−17] New technological applications in catalysis and bactericidal formulation have emerged for ZnO NPs due to their ability to generate reactive oxygen species by promoting H_2O dissociation, which has been investigated by DFT calculations.[17] The great affinity of H_2O molecules for ZnO, which induces the spontaneous dissociation of H_2O, is underlined by the study of the electronic properties of nearly spherical ZnO NPs with diameters ranging from 9 to 15 Å. The multifunctional behavior of ZnO particles is partly determined by the electronic structure, which depends on the size, shape, and crystallographic facets on the particle surfaces.[18−20] There are few studies on the electronic structural properties of differently prepared ZnO particles determined by the extended X-ray absorption fine structure (EXAFS) analysis.[21,22] Therefore, for highly technical, biomedical, or photocatalytic applications, the development of a size- and morphology-controlled ZnO synthesis route is of utmost importance. In particular, Šarić and co-workers[23−27] have reported in several recent papers a strong influence of the synthesis route on the formation of ZnO particles, their size, and geometrical shape. Nevertheless, among the various solution-based synthesis methods, the hydrothermal route is said to be attractive because of its simplicity.[28,29]

Anžlovar et al. studied the influence of various inorganic hydroxides on the formation and morphology of ZnO NPs.[30] The authors emphasized the molar ratio between hydroxide and the precursor, which plays an important role in the formation of ZnO. Several research studies have shown that a simple tuning of the NaOH/$Zn(acac)_2$ ratio[6,31] as well as the rate of addition of NaOH to the $Zn(acac)_2$ solution[32] can contribute to different growth mechanisms of ZnO nanostructures of different shapes and sizes. The most interesting results show that low and high concentrations of OH^- ions lead to ZnO growth in uniform and anisotropic directions, respectively, resulting in either spherical or anisotropic nanorods, while medium concentrations of OH^- ions contribute to a simultaneous mixing of both morphologies. When a relatively slow addition of OH^- occurred, the ZnO nanostructures grew in a uniform direction, leading to the formation of hexagonal prisms. However, if both precursor solutions (NaOH and $Zn(acac)_2$) were mixed simultaneously, the reaction would proceed faster and the growth along the [0001] direction would be more favorable. Undoubtedly, among these different shapes of ZnO nanostructures, a spherical-shaped ZnO exhibits the highest photocatalytic efficiency, which can be attributed to its large content of oxygen vacancies. Huang et al. found that the predominant facets of spherical ZnO NPs are polar {0001} facets.[33] In addition, the relationship between the particle size and the optical properties of ZnO NPs was investigated.[23,34] The redshift of the absorption edge and the decreased bandgap energies are clearly visible as the size of the microspheres increases.[23] Similarly, the defects in the ZnO nanorods due to the "oriented attachment" of the NPs are the reason for the redshifted absorption.[34] Numerous studies have been reported on the formation of hollow hexagonal tube-like and tower-like ZnO structures.[35−38] The authors emphasized the interesting correlation between the growth mechanisms of tower-like and tube-like ZnO. Among all the structured ZnO materials, hollow tubular structures are of great interest, which may provide opportunities for various new applications in catalysis, optical fibers,[39] and storage and release systems.[40] However, it is necessary to prepare tubular materials by a simple synthesis route under mild experimental conditions.[29] Regarding the possible growth mechanism of single-crystal tubular ZnO whiskers, Hu and Bando[41] explained a single crystallographic [0001] direction by the "lowest-energy argument" in which stacking along the hexagonal (001) plane of the wurtzite structure of ZnO as the most densely packed plane is energetically favorable.

In this article, we report a synergistic experimental and theoretical study of the growth mechanism and photocatalytic behavior of finely tuned hollow and nonhollow hierarchical ZnO structures. By changing the reaction medium from "pure" aqueous to aqueous alkaline NaOH solution and varying the aging time of the precursor solutions, the subtle differences in the microstructural and morphological features were elaborated by PXRD measurements and verified by comparative SEM and TEM micrographs. The effect of preparation conditions and aging time variation on the photocatalytic performance of the ZnO particles was monitored using degradation over the rhodamine B (RhB) dye pollutant solution. A complementary understanding of the microstructure of the differently prepared ZnO particles was obtained by a complex EXAFS data analysis and calculations at the DFT level, which filtered out the best ZnO candidates with the desired microstructural and morphological properties. The aim of the integrated experimental and theoretical approach was to gain a deeper insight into the formation and growth mechanism of the hierarchical ZnO structure, as well as to achieve a good control of its size and morphology in order to improve its photocatalytic activity.

METHODS AND MATERIALS

Materials and Synthesis. Zinc acetylacetonate monohydrate [$(Zn(C_5H_7O_2)_2{\cdot}H_2O$; 96%; Alfa Aesar, Germany] and sodium hydroxide (NaOH; Kemika reagent grade, 98%; Croatia) were used to prepare the samples. Milli-Q water was prepared in our laboratory. ZnO powder samples were prepared by a hydrothermal process. The sample notation and experimental conditions used for their preparation are given in Table 1. Figure 1 shows the flow chart of the preparation of the ZnO particles. In a typical synthetic procedure, zinc acetylacetonate monohydrate ($Zn(acac)_2$) was mixed in a predetermined amount with water (series A samples) or aqueous NaOH solution (series N samples), as described in our previous report.[29] The transparent precursor solution was autoclaved at 90 °C for up to 7 days. After an appropriate aging time, the obtained precipitate was separated from the supernatant using a centrifuge, additionally rinsed with ethanol and Milli-Q water, and then dried.

Powder X-ray Diffraction Measurements. PXRD data were collected in reflection mode with monochromatic Cu Kα radiation (λ = 1.54056 Å) using a Philips PW1880 diffractometer with a step size of 0.02° in the 2θ range between 25° and 80°. Crystal structure refinement was performed using the Rietveld algorithm[42] within the software GSAS II.[43] The crystallite sizes in the samples measured at

https://doi.org/10.1021/acs.inorgchem.1c03905
Inorg. Chem. 2022, 61, 2962−2979

Table 1. Summary of the Resulting Microstructural Parameters from Rietveld Refinements against PXRD Collected at RT, Together with the Observed Diffraction Intensity Ratio between (002) and (100) Bragg Reflections of the N and A Series Samples

sample	experimental conditions	aging time	crystallite size (nm)	lattice strains (%)	I_{002}/I_{100}
N1	2 g $Zn(acac)_2$ + 200 mL 1×10^{-3} M NaOH	1 day	33.6(1)	0.12(2)	0.33
N2	2 g $Zn(acac)_2$ + 200 mL 1×10^{-3} M NaOH	3 day	35.5(1)	0.12(1)	0.98
N3	2 g $Zn(acac)_2$ + 200 mL 1×10^{-3} M NaOH	7 day	42.9(1)	0.12(1)	0.45
N4	2 g $Zn(acac)_2$ + 200 mL 1×10^{-2} M NaOH	7 day	45.1(1)	0.12(1)	0.71
A1	2 g $Zn(acac)_2$ + 200 mL H_2O	1 day	20.9(1)	0.04(2)	1.10
A2	6 g $Zn(acac)_2$ + 200 mL H_2O	4 h	25.8(1)	0.13(1)	0.87

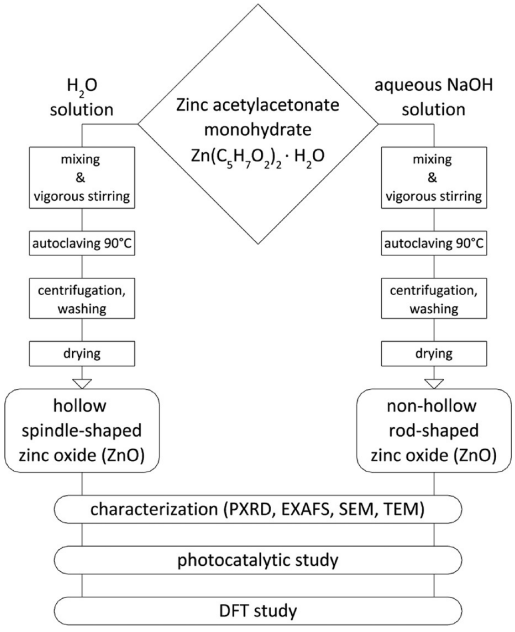

Figure 1. Schematic flow chart of the synthesis of ZnO particles.

room temperature (RT) were calculated using the phase-fitting method (i.e., simultaneously with the Rietveld structural refinements) based on the change in profile widths compared to a standard sample.

Morphology Characterization. The morphology of the synthesized samples was examined using field emission scanning electron microscopy (FESEM, model JSM-7000F) and Cs-corrected cold field emission scanning transmission electron microscopy (STEM, model ARM-200 CF) from Jeol Ltd. To minimize the beam damage, a low beam current and 80 keV electron energy were used. High-angle annular dark field (HAADF) images were acquired with 68−180 mrad collection half angles at 24 mrad probe convergence half angles. A Gatan Quantum ER dual electron energy-loss spectroscopy (EELS) and Jeol Centurio energy-dispersive X-ray spectroscopy (EDXS) system with a 100 mm^2 silicon drift detector (SDD) was used for chemical analysis. Powder samples were directly transferred to lacey carbon-coated nickel TEM grids.

X-ray Absorption Spectroscopy Study. The EXAFS experiments at the Zn K-edge (9659 eV) were performed at the materials science beamline BL10 at the 1.5 GeV synchrotron source DELTA (Dortmund, Germany), operating with 80−130 mA of stored current.[44] A Si(111) channel-cut monochromator was employed, and gas-filled ionization chambers were used to monitor the incident and the transmitted photon flux. Powder samples were homogeneously dispersed on adhesive Kapton (polyimide) tapes, and several tapes were stacked to obtain an absorption suited for X-ray absorption spectroscopy experiments. EXAFS scans were collected within typically 20 min acquisition time between ca. 200 eV below and about 1000 eV above the Zn K-edge, corresponding to a maximum photoelectron wavenumber of about k_{max} = 16.2 $Å^{-1}$, and three to five scans were averaged to improve the data statistics. For comparison, the reference spectra of Zn metal foil, hexagonal ZnO, solid $Zn(acac)_2$, and the precursor solution were measured as references. The data analysis comprised pre- and post-edge background subtraction and normalization transformation to the photoelectron wave vector (k) scale to extract the X-ray absorption fine structure $\chi(k)$ by employing the Athena software package.[45] The k^3-weighted EXAFS function was subjected to a Fourier transform and fitted with phases and scattering amplitudes calculated using the FEFF code,[46] assuming the crystallographic structure of wurtzite ZnO as the initial guess for the fits.

Photocatalysis Measurements. The photocatalytic activity of the ZnO catalysts was estimated through the degradation of RhB ($C_{28}H_{31}ClN_2O_3$; p. a., Merck) as a model organic dye. In a typical photocatalytic experiment, 10 mg of catalyst was dispersed in 50 mL of aqueous RhB solution (0.02 mM) and sonicated for 10 min. The suspension was kept in the dark under magnetic stirring (350 rpm) for 1 h to establish an adsorption−desorption equilibrium between the dye and the photocatalyst before illumination. Then, the lamps (8 W Hitachi) were switched on to initiate the photodegradation process. The reaction mixture was exposed to illumination between 300 and 600 nm and mixed by stirring (350 rpm) to maintain homogeneity. An aliquot of 2.5 mL reaction mixture was centrifuged at 5000 rpm and drawn through a syringe filter after appropriate illumination. The degradation of RhB was monitored by measuring the absorbance using UV−vis spectrophotometry (Varian Cary 50) in the wavelength range of 800−300 nm. After each measurement, the aliquot was returned to the reaction mixture.

Computational Details. The geometry optimization and calculation procedures were performed using DFT with the Gaussian 09 program (revision D1).[47] The M05-2X functional developed by Truhlar's group was selected.[48] The 6-31+G(d,p) basis set for H, C, and O atoms and the LANL2DZ basis set for Zn atoms were used for geometry optimization.[49] The final energies were refined using a highly flexible 6-311++G(2df,2pd) basis set for H, C, and O atoms, whereas the same LANL2DZ ECP basis set was used for Zn atoms. All geometry optimizations, frequency calculations, and single-point energy evaluations were performed, taking into account the solvent effects. The implicit solvation model based on density (SMD) polarizable continuum was used to evaluate the bulk solvent effects (water, ε = 78.4).[50] Topological analysis of the electron density distribution was performed with the AIMALL[51] software package using Bader's quantum theory of atoms in molecules (QTAIM).[52] The interactions and the nature of chemical bonding were characterized by the values of the Laplacian of the electron density $\nabla 2\rho(r_c)$ and the electron energy density $H(r_c)$ at the corresponding critical bonding point. The Gibbs free energies of the interactions, ΔG^*_{INT}, were calculated as the difference between the total free energy (G^*_{AB}) of the resulting structure (AB) and the sum of the total free energies ($G^*_A + G^*_B$) of the associating units. Further details of the calculations can be found in the Supporting Information.

RESULTS AND DISCUSSION

Phase Analysis and Microstructural Features. The resulting N and A series of white polycrystalline samples exhibited single-phase PXRD patterns at RT (Figure 2a), showing strong diffraction peaks that can be indexed to the hexagonal structure with space group symmetry $P6_3mc$ of the wurtzitic ZnO phase, which is in high agreement with standard data (PDF file no. 01-079-2205; a = 3.2501 Å; c = 5.2071 Å).[53] As can be seen from the Rietveld refinements (Figure 2b), a

https://doi.org/10.1021/acs.inorgchem.1c03905
Inorg. Chem. 2022, 61, 2962−2979

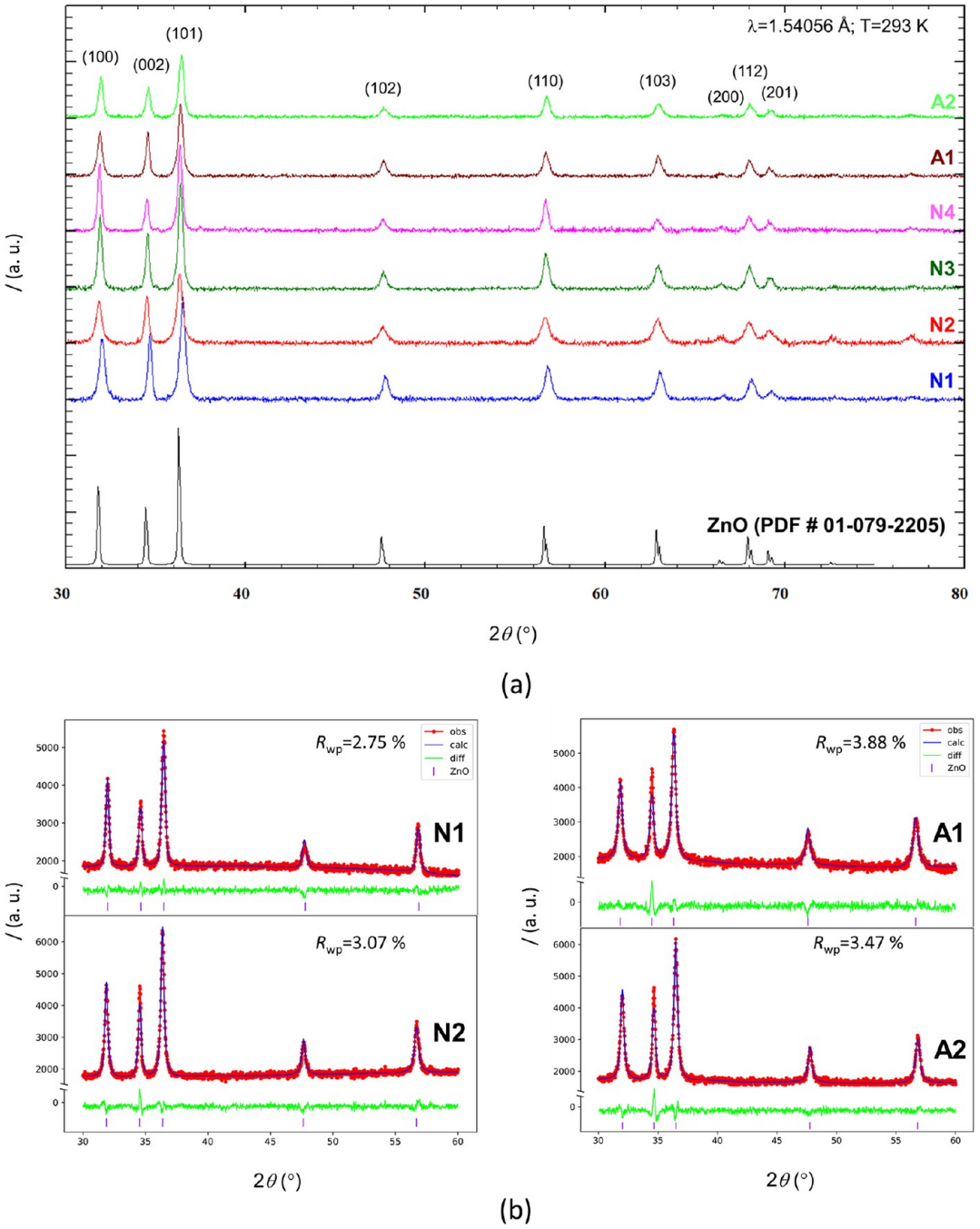

Figure 2. (a) Cascade PXRD patterns of series N and A samples taken at RT and (b) final observed (red dots) and calculated (blue solid lines) powder diffraction profiles for selected series N and A samples as obtained from Rietveld refinements by PXRD data. The lowest solid lines show the plots of difference between the measured and calculated diffraction profiles, while the purple vertical bars indicate the diffraction positions of Bragg.

good fitting can be obtained between the observed and calculated patterns.

The refinement procedure of the initial structure model[54] included refinement of the background parameters, preferred orientation, zero offset, lattice parameters *a* and *c*, position parameters *u*, and temperature factors for all atoms present. A pseudo-Voigt profile function and a log-normal background with up to nine coefficients were used in the structure refinements. Isotropic vibrational modes were assumed for all atoms. The resulting unit cell metrics are summarized in Table S1, along with reliability factors that confirm the validity of the refinement. Since the intensity of the diffraction peaks of the (101) crystal planes is the strongest, the *c*-oriented nature of the ZnO particles grown in an array seems to be the preferred one. Undoubtedly, an increase in aging rate and pH is followed by the uniform changes in I_{002}/I_{100} values due to the crystallite growth (Table 1).

In particular, by changing the aging time from 1 day to 7 days and increasing the pH, the crystallite size increased from 33.6(1) nm in sample N1 to 45.1(1) nm in sample N4. The experimental conditions and aging rates did not significantly affect the lattice microstrain of the samples prepared in alkaline

https://doi.org/10.1021/acs.inorgchem.1c03905
Inorg. Chem. 2022, 61, 2962−2979

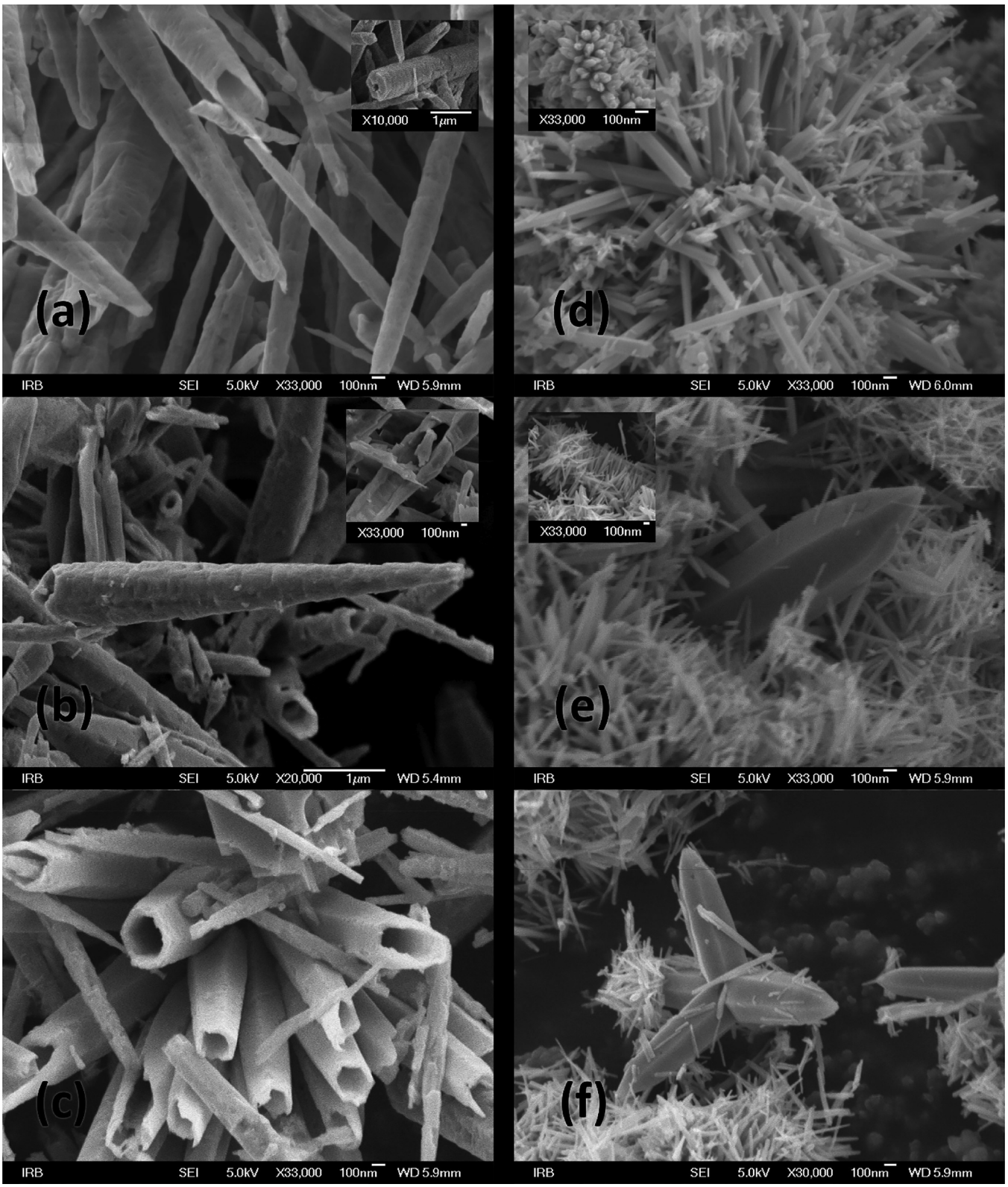

Figure 3. FESEM images of ZnO samples prepared in aqueous NaOH solution (left panel): (a) N1, (b) N2, and (c) N4; FESEM images of ZnO samples prepared in "pure" aqueous solution (right panel): (d) A1 and (e, f) A2 at different magnifications.

media, so the uniform value of 0.12% was retained. In contrast, in "pure" aqueous solution, the addition of a higher reactant content (sample A2) resulted in an increase in the lattice microstrain from 0.04(2)% in sample A1 to 0.13(1)% in sample A2, approaching the values observed in the alkaline medium. Different experimental conditions and aging times applied in the preparation of series A resulted in a slight change in the crystallite sizes with the increase in the amount of $Zn(acac)_2$ added to the solution. Interestingly, by comparing the data in Table S1 and Table 1, a correlation can be

https://doi.org/10.1021/acs.inorgchem.1c03905
Inorg. Chem. 2022, 61, 2962−2979

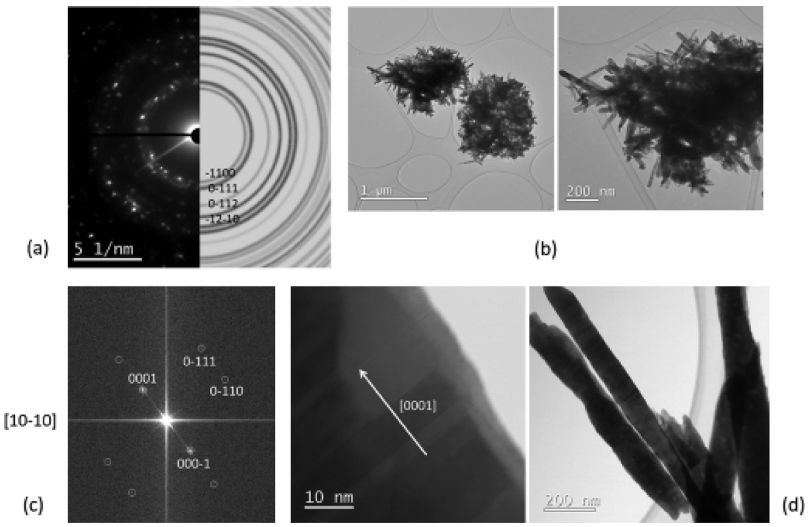

Figure 4. Sample A1 prepared in "pure" aqueous solution: (a) experimental and simulated SAED patterns for hexagonal ZnO and (b) TEM images at different magnifications. Sample N1 prepared in aqueous NaOH solution: (c) FFT of BF-STEM image and (d) BF-STEM micrographs at different magnifications.

established between the unit cell parameters and the estimated microstructural trend observed in the series N samples—the larger the unit cell parameters, the more pronounced the increase in crystallite size.

Surface Morphology Imaging. The general morphologies of the ZnO particles in the samples are summarized in selected representative SEM images in Figure 3. The SEM images of ZnO particles prepared by the hydrolysis of $Zn(acac)_2$ in aqueous NaOH solution are shown in the left panels of Figure 3, while the right side of Figure 3 shows SEM micrographs of particles prepared in "pure" aqueous solution.

Indeed, significant differences in size and morphology between ZnO particles obtained in "pure" aqueous solution on one side and in aqueous NaOH solution on the other side are well visible. Regardless of the differences, all SEM images show ZnO particles with geometrical shapes corresponding to the hexagonal space group of wurtzite but with subtle and clearly visible differences depending on the reaction medium. The SEM images of ZnO particles prepared in the aqueous NaOH solution show the formation of hollow spindle-shaped hierarchical microstructures tapering at one end (Figure 3a–c). The formation of hollow tubular structures with an average length of several micrometers is dependent on both the aging time and the concentration of NaOH solution. The basis of the large particles shows that the particles with an average length of several micrometers were formed by stacking of ZnO nanostructures, thus pointing to the strong tendency for hierarchical lamellar aggregation. It can be seen that hollow spindle-shaped particles in the aqueous NaOH solution grow layer by layer with lamellar hexagonal stacks. The hollow spindle-shaped particle shown in Figure 3b is about 5 μm long and has a diameter between the end and the top of the particle in the range of about 100–500 nm. The diameter of the craters of the hollow tubular structures changes with aging time and concentration of NaOH solution. As can be seen in the inset of Figure 3a, the spindle-shaped ZnO particles prepared at 1×10^{-3} M NaOH for an aging time of 1 day have small craters at the top. For longer reaction times, when the reaction lasts for 3 days, the wall thickness of the spindle-shaped structure becomes thinner (Figure 3b). The inset in Figure 3b is a magnified image showing one half of the cracked hollow spindle tube. It can be seen that the fully hollow interior of the microstructures consists of layered lamellar substructures with an average layer length of ~100–200 nm. The easier cracking of large hollow structures is probably due to the thinner wall thickness. When the NaOH concentration increases from 1×10^{-3} (Figure 3a,b) to 1×10^{-2} (Figure 3c), the craters become larger and transform into hollow hexagonal microstructures with thinner wall thicknesses. Moreover, a longer reaction time of up to 7 days and an increase in NaOH concentration to 1×10^{-2} M NaOH lead to the smoothness of the facets of ZnO particles (Figure 3c). Additionally, a hollow hexagon as a stable geometric shape is shown in Figure 3c. The visible layered nanosheet substructure indicates that the hollow spindle-shaped ZnO microstructure is formed layer by layer from a lamellar hexagonal stacking structure in the presence of NaOH.

On the other hand, nonhollow, thinner, and elongated ZnO microstructures are observed in "pure" aqueous solution by hydrolysis of 2 g of $Zn(acac)_2$ for 1 day aging time (see Figure 3d). A detailed inspection of the FESEM image shown in Figure 3d reveals that the ZnO particles are several micrometers in size and have a high aspect ratio. In addition, the tips of the rods can be seen to taper into needles with a smooth surface. The insets in Figure 3d,e reveal the mechanism of crystal growth by stacking thin, elongated, and laterally arranged ZnO nanorods. The selected representative SEM images of the ZnO particles synthesized in aqueous solution with the higher starting contents of $Zn(acac)_2$ (6 g) for 4 h aging time point out the presence of thin elongated rods as well as giant hexagonal pyramidal prisms (Figure 3e,f). It can be seen that the thermodynamically unstable acicular ZnO crystals transform into giant prismatic pyramidal structures with increasing content of $Zn(acac)_2$. Moreover, a coalescence of these giant prismatic pyramidal structures with a common basal plane is observed (see Figure 3f). In addition, the arrangement of discrete, thin, and elongated nanorods can be clearly seen in the inset of Figure 3e. Apparently, the preferential crystal growth along the *c*-axis is represented by the stacking of thin, elongated, and laterally arranged ZnO nanorods in "pure" aqueous solution. In summary, the observed FESEM results indicate a different formation and growth mechanism, highlighting the tendency for lateral

https://doi.org/10.1021/acs.inorgchem.1c03905
Inorg. Chem. 2022, 61, 2962–2979

stacking of nanorods during preferential crystal growth in "pure" aqueous solution compared to hierarchical lamellar stacking of nanodiscs in the aqueous NaOH medium. The formation of hollow tubular and tower-like ZnO structures has been reported by many researchers as this morphology is important for practical applications.[35,36] Among all pathways, the solution chemical route has emerged as a promising option for large-scale fabrication of 1D nano- and microstructured materials due to its simple, fast, and cheaper variants.[55]

The growth of ZnO particles was examined via transmission electron microscopy. The TEM/STEM micrographs of ZnO particles of A and N series are shown in Figure 4. The prismatic NPs in sample A1 are randomly oriented in bundles (Figure 4b) as seen from the selected area electron diffraction (SAED) pattern consisting of diffraction spots more or less uniformly distributed in parallel circles (Figure 4a). The individual NPs in sample N1 are elongated in the [0001] direction, as shown in Figure 4c,d. The contrast differences in the STEM micrograph (Figure 4d) indicate the planar defects parallel to the basal planes (possibly stacking faults or inversion domain boundaries).

Photocatalytic Activity. In this study, the photocatalytic activity of the as-prepared ZnO particles was investigated using the degradation of rhodamine B as a model for an organic dye pollutant. The UV−vis adsorption spectra of RhB solution as a function of illumination time (up to 180 min) in the presence of all prepared ZnO photocatalysts are shown in the Supporting Information (Figure S1). It can be seen that the main absorption peak at 554 nm for RhB decreases significantly with irradiation time when ZnO photocatalysts are added, especially those prepared in "pure" aqueous solution. The corresponding concentration changes of RhB solution during the degradation process in the presence of three selected types of ZnO photocatalysts (samples A1, A2, and N1) are shown in Figure 5a. It was found that the photocatalytic degradation of RhB over ZnO catalysts prepared in aqueous solution (samples A1 and A2) is much faster and higher than that in aqueous NaOH solution (samples N1−N4, see Figure S2). Samples A1 and A2 degraded the RhB solution by 70 and 76%, respectively, in 120 min. On the other hand, only 23% of RhB dye is degraded by hollow spindle-shaped ZnO particles in sample N1 (Figure 3b). The photodegradation of RhB over ZnO photocatalysts (see Figure 5a) proceeds by a pseudo-first-order kinetic reaction through linear transformations $\ln(c_0/c_t) = kt$, where c_t and c_0 are the concentrations of RhB at different illumination times, and k is the photodegradation constant ranging from 0.0028 to 0.0106 min^{-1} and decreasing in the order A2 > A1 > N1. It is well known that the photocatalytic activity of ZnO catalysts is determined by their nano- and microstructure. These morphological and structural differences are reflected in the significant changes in photocatalytic activity described above, as estimated by the higher and faster degradation of RhB over ZnO samples prepared in "pure" aqueous solution compared to those obtained in aqueous NaOH solution. A synergistic effect between the ratio I_{002}/I_{100} and the crystallite size on the photocatalytic activity is revealed. The higher the ratio I_{002}/I_{100}, the higher the catalytic activity should be expected.

There are some publications discussing the relationship between the photocatalytic activity of ZnO and the observed ratio of the intensities of the (002) and (100) Bragg reflections.[56−58] Kovács et al.[56] found that the increased ratio of (002) to (100) Bragg reflections greatly improves the

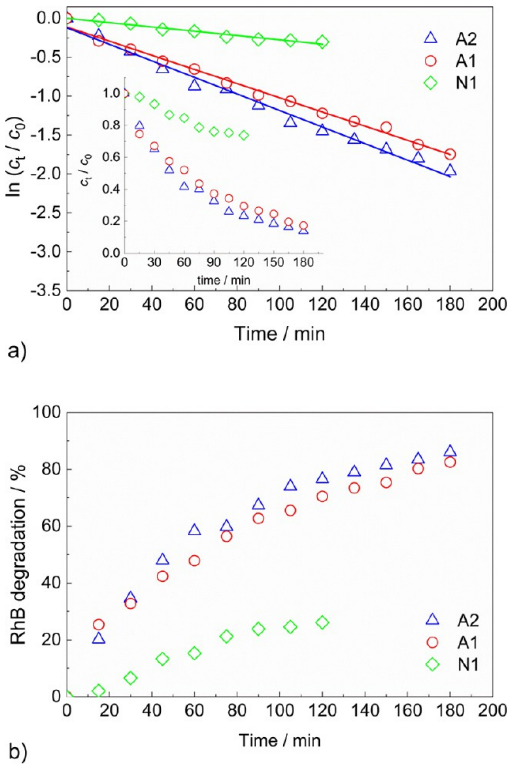

Figure 5. (a) Photocatalytic degradation of RhB over samples A1, A2, and N1 under UV light illumination and (b) photocatalytic efficiency of RhB degradation determined for samples A1, A2, and N1.

photocatalytic activity of the ZnO samples, which is related to the water content of the solvent. The higher the ethanol content, the less water molecules can be adsorbed on the specific crystallographic planes. The high water concentration could inhibit growth toward a polar crystal facet of ZnO. The terminal Zn^{2+} and O^{2-} molecules along the (002) crystal plane may interact strongly with the polar H_2O molecules in their dislocated form (OH^- and H^+). The photocatalytic reaction occurs at the interface, which requires effective adsorption of the reaction molecules/ions on the surface of the ZnO photocatalysts. Since the adsorption states of certain molecules/ions are determined by the atomic surface structures of ZnO, the photocatalytic efficiency is related to the electronic structure and shape of ZnO.[33,59] Thus, the difference in the atomic structure of the surface as well as the different surface area may explain the discrepancy in the ability of chemisorbed oxygen or hydroxyl species, which consequently affects the photocatalytic efficiency of the ZnO particles. It seems that the higher photocatalytic activity of thin ZnO rods and needles prepared in "pure" aqueous solution is due to the presence of a larger amount of surface oxygen or hydroxyl species, as well as a larger surface area due to the smaller particle size, compared to those obtained in aqueous NaOH solution.

The large affinity of H_2O molecules for ZnO, leading to the spontaneous dissociation of H_2O, is highlighted by the Petridis research group.[17] This study highlights the importance of the surface arrangement of Zn and O atoms on the facets and edges of the NPs, which leads to adsorption sites with different local electronic structures and thus does not provide equivalent sites for molecular or spontaneous dissociative adsorption. The authors emphasized that the presence of dangling bonds

https://doi.org/10.1021/acs.inorgchem.1c03905
Inorg. Chem. 2022, 61, 2962−2979

resulting from the transformation of the ZnO crystal into an NP with facets leads to a favorable electronic environment and induces the spontaneous dissociation of H_2O. The authors suggested that the synthesis of NPs with an increased number of edges as well as reactive oxygen species leads to spontaneous dissociation of H_2O compared to the macroscopic ZnO surface, which prevents the spontaneous dissociation of a single H_2O. Gupta et al. investigated the defect-induced photocatalytic activity of ZnO nanostructures due to different shapes obtained by varying the concentration of OH^- ions.[6] The authors suggest that the higher photocatalytic activity is due to the presence of a larger amount of point defects such as oxygen vacancies on the surface of the ZnO nanostructures.

EXAFS Study. However, much more structural information is needed to understand the relationship between the detailed crystal structure and the physicochemical properties, especially the photocatalytic properties. Reliable experimental confirmation of the XAS measurements enabled suggestions for general conclusions regarding the photocatalytic efficiency of the ZnO samples. Therefore, to reveal the electronic structure of differently prepared ZnO particles, the contributions of EXAFS data analysis must be taken into account. Erat et al.[22] investigated the electronic and local crystal structure of micrometer-sized ZnO and ZnO:B synthesized by a hydrothermal method using EXAFS and XANES techniques. Since the photocatalytic performances are strongly correlated with the electronic structure, size, and shape of ZnO, the correlation of EXAFS results with the photocatalytic degradation results of organic dye pollutants such as RhB with ZnO particles of different sizes and morphologies provides a comprehensive understanding of the relationship between structural details and photocatalytic activity.

Therefore, we have analyzed the Zn K-edge EXAFS of the different samples A1, A2, and N1. In Figure 6, the magnitudes of the Fourier transforms of the k^3-weighted EXAFS fine structures $\chi(k)$ are compared. First of all, it should be noted that the data of all the investigated samples agree qualitatively with the structure of hexagonal wurtzite ZnO (see, e.g., ref 22). As can be seen, the amplitudes of the Zn−O shell at about 1.6 Å radial distance and the Zn−Zn peak at 2.9 Å are the most intense for sample N1, with decreasing intensity for sample A1 and even smaller values for A2. This implies that the nanostructure of the synthesized particles obviously depends on the details of the preparation. For the quantitative EXAFS data evaluation, we have performed a fit assuming the hexagonal space group no. 186 ($P6_3mc$) with lattice parameters as provided in Table S1 as the initial guess for the structure. All Zn and O atoms up to a radius of 4.7 Å were considered for the fit here, resulting in a cluster with 14 different single and multiple scattering paths and a total of 39 atoms. In principle, each of the considered scattering paths is related to a coordination shell (i), which is characterized by its distance R_i, the number of atoms in the shell (N_i), the amplitude reduction factor ($S_{0,i}^2$), the inner potential shift (ΔE_{0i}), and the mean square displacement (σ_i^2). If all of the above-mentioned shells were treated individually, the result would be a huge and statistically insignificant number of fit variables. The limit for the number of fit variables (N_{ipd}) can be estimated from the energy range measured during the experiment, the k-range used for the Fourier transform (here, the range from k_{min} = 2.540 Å^{-1} to k_{max} = 14.342 Å^{-1}), and the R-range in the FT used for the fit (here, R_{min} = 1.1 Å to R_{max} = 4.5 Å); for details see, e.g., ref 60. For the present experiments, N_{idp} is in the range of 25, i.e., a maximum of 25 fit variables would be statistically justifiable to be used.

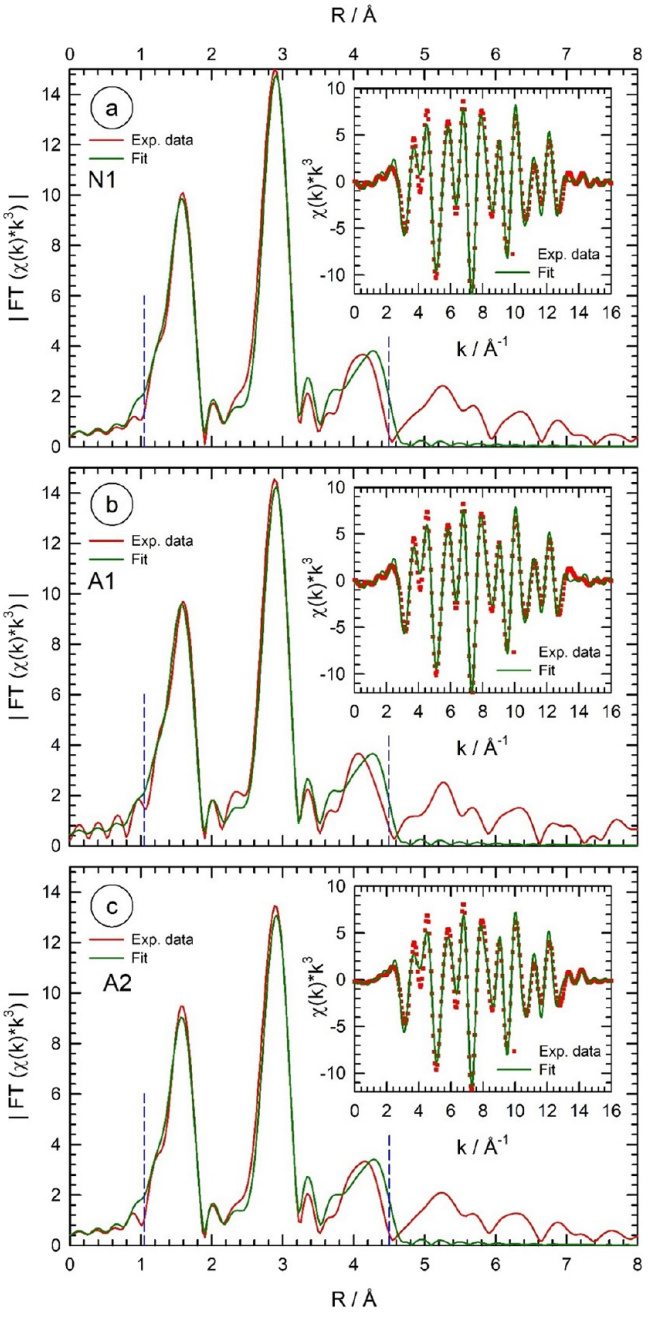

Figure 6. Magnitudes of the Fourier transform of the k^3-weighted EXAFS fine structure |FT ($\chi(k)$*k^3)| for (a) N1, (b) A1, and (c) A2. Both the raw data and the fits to the wurtzite structure are shown. The insets depict the back transform ($\chi(k)$*k^3 data) of the Fourier transform in the range from R_{min} = 1.1 Å to R_{max} = 4.5 Å (dashed vertical blue lines) for the data and the fits. More details are provided in the text (k-range for the Fourier transform: k_{min} = 2.540 Å^{-1} to k_{max} = 14.342 Å^{-1}).

Thus, for the quantitative fitting of our experimental EXAFS data, we have developed a model with a substantially smaller number of fit variables, i.e., we have varied the distances R_1 (i.e., Zn−O) and R_2 (i.e., Zn−Zn) individually to detect the small change of the first- and second-neighbor bonds more sensitively, while all other distances were fitted with a single scaling factor α so that the fitted distance for all paths beyond

https://doi.org/10.1021/acs.inorgchem.1c03905
Inorg. Chem. 2022, 61, 2962−2979

Table 2. Compilation of EXAFS Fit Results from Samples N1, A1, and A2[a]

		sample N1			sample A1			sample A2		
		R-factor: 0.0525, α = −0.0158 ± 0.0022			*R*-factor: 0.0523, α = −0.0170 ± 0.0022			*R*-factor: 0.0519, α = −0.0158 ± 0.0022		
path	N_i	$S_{0,i}^2$	$\sigma_i^2/10^{-3}$ Å^2	R_i/Å	$S_{0,i}^2$	$\sigma_i^2/10^{-3}$ Å^2	R_i/Å	$S_{0,i}^2$	$\sigma_i^2/10^{-3}$ Å^2	R_i/Å
Zn−O	4	0.92 ± 0.14	5.42 ± 1.40	1.973 ± 0.008	0.90 ± 0.13	5.47 ± 1.38	1.972 ± 0.008	0.82 ± 0.12	5.05 ± 1.29	1.972 ± 0.007
Zn−Zn	12	0.98 ± 0.14	9.31 ± 2.42	3.240 ± 0.004	0.95 ± 0.06	9.31 ± 2.04	3.239 ± 0.004	0.83 ± 0.05	8.96 ± 2.23	3.241 ± 0.004
Zn−O	1	0.92 ± 0.14	5.42 ± 1.40	3.242 ± 0.007	0.90 ± 0.13	5.47 ± 1.38	3.238 ± 0.007	0.90 ± 0.13	5.05 ± 1.29	3.242 ± 0.007
Zn−O−O	12	0.92 ± 0.14	5.42 ± 1.40	3.587 ± 0.008	0.90 ± 0.13	5.47 ± 1.38	3.582 ± 0.008	0.90 ± 0.13	5.05 ± 1.29	3.587 ± 0.008
Zn−O−Zn	24	0.95 ± 0.10	7.36 ± 1.91	3.587 ± 0.008	0.93 ± 0.09	7.47 ± 1.71	3.582 ± 0.008	0.93 ± 0.09	7.00 ± 1.76	3.587 ± 0.008
Zn−O	9	0.92 ± 0.14	5.42 ± 1.40	3.793 ± 0.009	0.90 ± 0.13	5.47 ± 1.38	3.789 ± 0.009	0.90 ± 0.13	5.05 ± 1.29	3.794 ± 0.009
Zn−O	4	0.92 ± 0.14	5.42 ± 1.40	3.949 ± 0.009	0.90 ± 0.13	5.47 ± 1.38	3.944 ± 0.009	0.90 ± 0.13	5.05 ± 1.29	3.949 ± 0.009
Zn−O−Zn−O	12	0.94 ± 0.11	6.72 ± 1.73	3.949 ± 0.009	0.92 ± 0.09	6.80 ± 1.60	3.944 ± 0.009	0.92 ± 0.09	6.35 ± 1.60	3.949 ± 0.009
Zn−O−O	6	0.92 ± 0.14	5.42 ± 1.40	4.213 ± 0.009	0.90 ± 0.13	5.47 ± 1.38	4.208 ± 0.009	0.90 ± 0.13	5.05 ± 1.29	4.213 ± 0.009
Zn−O−Zn	36	0.95 ± 0.10	7.36 ± 1.91	4.499 ± 0.010	0.93 ± 0.09	7.47 ± 1.71	4.493 ± 0.010	0.93 ± 0.09	7.00 ± 1.76	4.499 ± 0.010
Zn−O−O	36	0.92 ± 0.14	5.42 ± 1.40	4.499 ± 0.010	0.90 ± 0.13	5.47 ± 1.38	4.493 ± 0.010	0.90 ± 0.13	5.05 ± 1.29	4.499 ± 0.010
Zn−Zn−O	36	0.95 ± 0.10	7.36 ± 1.91	4.499 ± 0.010	0.93 ± 0.09	7.47 ± 1.71	4.493 ± 0.010	0.93 ± 0.09	7.00 ± 1.76	4.499 ± 0.010
Zn−Zn	6	0.98 ± 0.06	9.31 ± 2.42	4.560 ± 0.010	0.95 ± 0.06	9.31 ± 2.04	4.553 ± 0.010	0.95 ± 0.06	8.96 ± 2.23	4.560 ± 0.010
Zn−O	6	0.92 ± 0.14	5.42 ± 1.40	4.582 ± 0.010	0.90 ± 0.13	5.47 ± 1.38	4.575 ± 0.010	0.90 ± 0.13	5.05 ± 1.29	4.582 ± 0.010

[a]For the different path with the number of scatterers (N_i) as indicated, the amplitude reduction factors $S_{0,i}^2$, the mean square displacement σ_i^2, and the bond length R_i were determined by the fits. While the two first shells were fitted with individual $S_{0,i}^2$ and R_i, a lattice expansion factor α was employed for all other shells, and Zn−O and Zn−Zn coordinations got identical $S_{0,i}^2$ values. The inner potential shift was refined for all samples simultaneously with a value of ΔE_0 = 4.888 ± 0.748 eV. See the text for more details.

https://doi.org/10.1021/acs.inorgchem.1c03905
Inorg. Chem. 2022, 61, 2962−2979

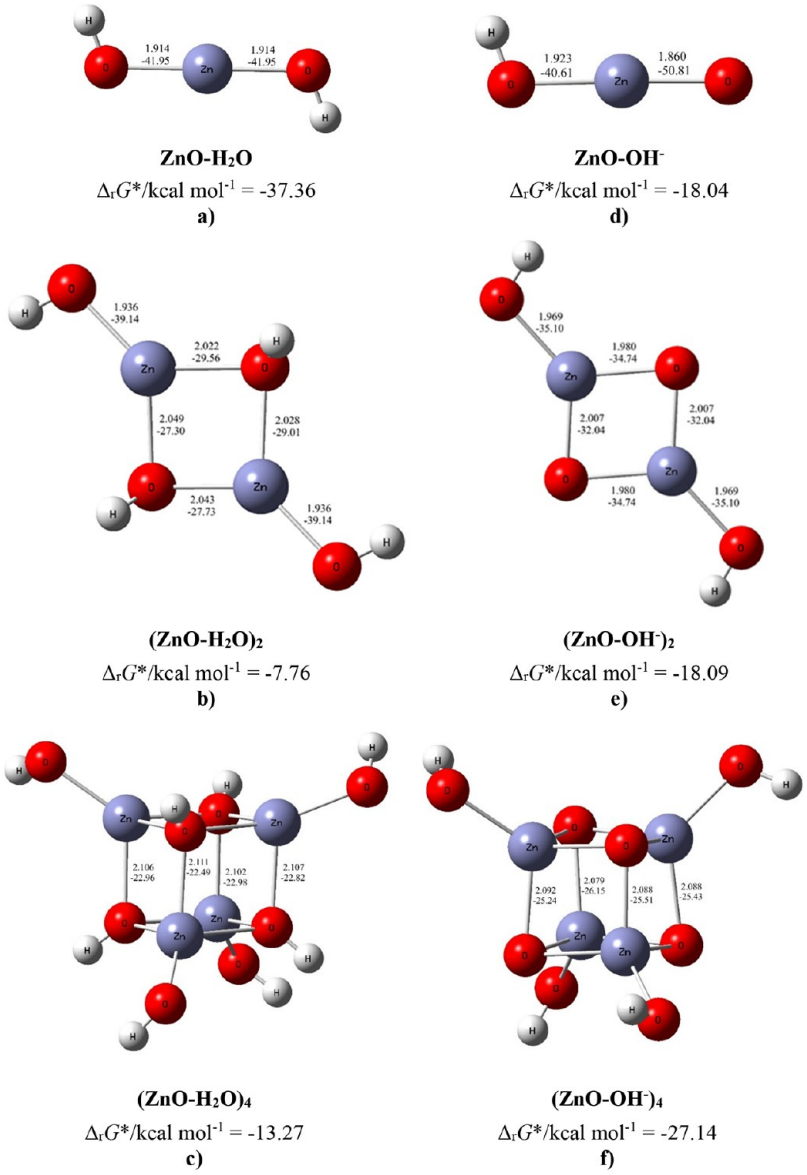

Figure 7. Most stable structures of ZnO−H_2O and ZnO−OH^- monomers, dimers, and tetramers (the bond distances are in Å, and the bond energies are in kcal mol^{-1}).

the first two shells is given by R_{eff}*α, with R_{eff} being the distance calculated from the original crystal structure (see above). All Zn−O coordinations were fitted using the same σ_O^2 and all Zn−Zn bonds with σ_{Zn}^2. For multiple scattering pathways, the average values of the respective shells were used. The same approach was used for the amplitude reduction factors $S_{0,i}^2$, i.e., all Zn−O and Zn−Zn shells were weighted with the same values for $S_{0,i}^2$, respectively, and multiple scattering paths were again weighted according to the involved atoms using the number of atoms N_i according to the hexagonal structure. To minimize the influence of the correlation of the inner potential shift (ΔE_{0i}) and all the distances, we have used the same value for ΔE_0 for all samples and all shells. By optimizing all three data sets simultaneously, we have derived a value of ΔE_0 = 4.888 ± 0.748 eV. In total, therefore, only seven variables were optimized individually for the three samples, while one parameter was optimized for all three. Quantitative fit results are included in Figure 6 and are compiled in the subsequent Table 2. The most important trend is that the obtained values for S_0^2 are the smallest (also if the fit errors are included) for sample A2, with the highest reactivity for RhB degradation, followed by sample A1 and sample N1, which showed the lowest performance in RhB degradation, with the largest values for $S_{0.}^2$

The reduced values obtained for the amplitude reduction factors for the samples prepared in pure aqueous solutions, in particular for sample A2, may be related to the presence of several O and Zn deficiencies, most probably on the surface of the nanostructured ZnO particles. Compared to N1, SEM micrographs suggest a more nanostructured surface for A1 and A2 so that the contributions of the surfaces with accordingly missing atoms are pronounced, leading to effectively lower coordination numbers and amplitude reduction factors accordingly. Therefore, the highest reactivity for RhB degradation observed for the ZnO samples prepared in "pure" aqueous media can be correlated with EXAFS analysis and reflects an improved photocatalytic performance compared to the samples prepared in aqueous NaOH solution. According

https://doi.org/10.1021/acs.inorgchem.1c03905
Inorg. Chem. 2022, 61, 2962−2979

Table 3. Bond Lengths (d), Energies (E), and QTAIM Properties of the Selected Bonds in the Most Stable Monomers, Dimers, and Tetramers of the Investigated Systems in the Water Solvent

			ZnO−H_2O				
bond	d/Å	$\rho(r_c)/e \times a_0^{-3}$	$\nabla^2\rho(r_c)/e \times a_0^{-5}$	$V(r_c)$/au	$G(r_c)$/au	$H(r_c)$/au[a]	E/kcal mol^{-1}[b]
O(1)−Zn(2)	1.914	8.379×10^{-2}	0.4827	−0.1337	0.1272	−0.0065	−41.95
Zn(2)−O(3)	1.914	8.379×10^{-2}	0.4827	−0.1337	0.1272	−0.0065	−41.95
			$(ZnO-H_2O)_2$				
bond	d/Å	$\rho(r_c)/e \times a_0^{-3}$	$\nabla^2\rho(r_c)/e \times a_0^{-5}$	$V(r_c)$/au	$G(r_c)$/au	$H(r_c)$/au	E/kcal mol^{-1}
O(1)−Zn(2)	1.936	7.907×10^{-2}	0.4493	−0.1247	0.1185	−0.0062	−39.14
Zn(2)−O(3)	2.022	6.415×10^{-2}	0.3278	−0.0942	0.0809	−0.0061	−29.56
Zn(2)−O(6)	2.049	6.063×10^{-2}	0.2944	−0.0870	0.0803	−0.0067	−27.30
O(3)−Zn(5)	2.028	6.324×10^{-2}	0.3199	−0.0925	0.0862	−0.0062	−29.01
O(6)−Zn(5)	2.043	6.138×10^{-2}	0.3005	−0.0884	0.0817	−0.0066	−27.73
Zn(5)−O(4)	1.936	7.907×10^{-2}	0.4493	−0.1247	0.1185	−0.0062	−39.14
			$(ZnO-H_2O)_4$				
bond	d/Å	$\rho(r_c)/e \times a_0^{-3}$	$\nabla^2\rho(r_c)/e \times a_0^{-5}$	$V(r_c)$/au	$G(r_c)$/au	$H(r_c)$/au	E/kcal mol^{-1}
Zn(1)−O(2)	2.102	5.224×10^{-2}	0.2370	−0.0732	0.0662	−0.0070	−22.98
O(3)−Zn(4)	2.107	5.227×10^{-2}	0.2326	−0.0727	0.0654	−0.0073	−22.82
O(5)−Zn(6)	2.107	5.255×10^{-2}	0.2338	−0.0732	0.0658	−0.0074	−22.96
Zn(7)−O(8)	2.111	5.138×10^{-2}	0.2289	−0.0717	0.0645	−0.0072	−22.49
			$(ZnO-H_2O)_8$				
bond	d/Å	$\rho(r_c)/e \times a_0^{-3}$	$\nabla^2\rho(r_c)/e \times a_0^{-5}$	$V(r_c)$/au	$G(r_c)$/au	$H(r_c)$/au	E/kcal mol^{-1}
H(1)−O(2)	1.724	4.322×10^{-2}	0.1282	−0.0346	0.0333	−0.0013	−10.86
O(3)−H(4)	1.707	4.549×10^{-2}	0.1332	−0.0370	0.0351	−0.0018	−11.60
O(5)−H(6)	1.736	4.212×10^{-2}	0.1253	−0.0337	0.0325	−0.0019	−10.57
H(7)−O(8)	1.801	3.668×10^{-2}	0.1092	−0.0290	0.0282	−0.0009	−9.10
			$(ZnO-H_2O)_{12}$				
bond	d/Å	$\rho(r_c)/e \times a_0^{-3}$	$\nabla^2\rho(r_c)/e \times a_0^{-5}$	$V(r_c)$/au	$G(r_c)$/au	$H(r_c)$/au	E/kcal mol^{-1}
H(1)−O(2)	1.780	3.783×10^{-2}	0.1132	−0.0296	0.0290	−0.0007	−9.29
O(3)−H(4)	1.735	4.235×10^{-2}	0.1257	−0.0339	0.0327	−0.0012	−10.63
O(5)−H(6)	1.703	4.572×10^{-2}	0.1349	−0.0374	0.0356	−0.0018	−11.73
H(7)−O(8)	1.715	4.462×10^{-2}	0.1314	−0.0362	0.0342	−0.0017	−11.36
H(9)−O(10)	1.766	3.925×10^{-2}	0.1185	−0.0312	0.0304	−0.0008	−9.79
O(11)−H(12)	1.744	4.106×10^{-2}	0.1246	−0.0329	0.0320	−0.0009	−10.31
O(13)−H(14)	1.703	4.543×10^{-2}	0.1344	−0.0370	0.0353	−0.0017	−11.61
H(15)−O(16)	1.749	4.089×10^{-2}	0.1234	−0.0328	0.0318	−0.0010	−10.28
			ZnO−OH^-				
bond	d/Å	$\rho(r_c)/e \times a_0^{-3}$	$\nabla^2\rho(r_c)/e \times a_0^{-5}$	$V(r_c)$/au	$G(r_c)$/au	$H(r_c)$/au[a]	E/kcal mol^{-1}[b]
O(1)−Zn(2)	1.860	9.796×10^{-2}	0.5606	−0.1619	0.1510	−0.0109	−50.81
Zn(2)−O(3)	1.923	8.209×10^{-2}	0.4643	−0.1294	0.1228	−0.0067	−40.61
			$(ZnO-OH^-)_2$				
bond	d/Å	$\rho(r_c)/e \times a_0^{-3}$	$\nabla^2\rho(r_c)/e \times a_0^{-5}$	$V(r_c)$/au	$G(r_c)$/au	$H(r_c)$/au	E/kcal mol^{-1}
O(1)−Zn(2)	1.969	7.332×10^{-2}	0.3974	−0.1119	0.1056	−0.0063	−35.10
Zn(2)−O(3)	1.980	7.395×10^{-2}	0.3778	−0.1107	0.1026	−0.0081	−34.74
Zn(2)−O(6)	2.007	6.965×10^{-2}	0.3419	−0.1021	0.0938	−0.0083	−32.04
O(3)−Zn(5)	2.007	6.965×10^{-2}	0.3419	−0.1021	0.0938	−0.0083	−32.04
O(6)−Zn(5)	1.980	7.395×10^{-2}	0.3778	−0.1107	0.1026	−0.0081	−34.74
Zn(5)−O(4)	1.969	8.523×10^{-2}	0.4933	−0.1371	0.1302	−0.0069	−43.03
			$(ZnO-OH^-)_4$				
bond	d/Å	$\rho(r_c)/e \times a_0^{-3}$	$\nabla^2\rho(r_c)/e \times a_0^{-5}$	$V(r_c)$/au	$G(r_c)$/au	$H(r_c)$/au	E/kcal mol^{-1}
Zn(1)−O(2)	2.088	5.863×10^{-2}	0.2496	−0.0811	0.0717	−0.0093	−25.43
O(3)−Zn(4)	2.088	5.867×10^{-2}	0.2508	−0.0813	0.0721	−0.0093	−25.51
O(5)−Zn(6)	2.079	5.962×10^{-2}	0.2600	−0.0833	0.0742	−0.0092	−26.15
Zn(7)−O(8)	2.092	5.815×10^{-2}	0.2469	−0.0805	0.0711	−0.0094	−25.24
			$(ZnO-OH^-)_8$				
bond	d/Å	$\rho(r_c)/e \times a_0^{-3}$	$\nabla^2\rho(r_c)/e \times a_0^{-5}$	$V(r_c)$/au	$G(r_c)$/au	$H(r_c)$/au	E/kcal mol^{-1}
H(1)−O(2)	1.907	3.032×10^{-2}	0.0823	−0.0239	0.0222	−0.0017	−7.50
O(3)−H(4)	1.898	3.212×10^{-2}	0.0888	−0.0254	0.0238	−0.0016	−7.98
O(5)−H(6)	1.933	2.862×10^{-2}	0.0769	−0.0226	0.0209	−0.0017	−7.08
H(7)−O(8)	1.913	2.981×10^{-2}	0.0809	−0.0235	0.0219	−0.0016	−7.38

https://doi.org/10.1021/acs.inorgchem.1c03905
Inorg. Chem. 2022, 61, 2962−2979

Table 3. continued

		$(ZnO-OH^-)_{12}$					
bond	d/Å	$\rho(r_c)/e \times a_0^{-3}$	$\nabla^2\rho(r_c)/e \times a_0^{-5}$	$V(r_c)$/au	$G(r_c)$/au	$H(r_c)$/au	E/kcal mol^{-1}
H(1)−O(2)	1.892	3.115×10^{-2}	0.0854	−0.0245	0.0229	−0.0016	−7.69
O(3)−H(4)	1.874	3.219×10^{-2}	0.0896	−0.0254	0.0239	−0.0015	−7.98
O(5)−H(6)	1.884	3.156×10^{-2}	0.0871	−0.0249	0.0233	−0.0016	−7.82
H(7)−O(8)	1.885	3.168×10^{-2}	0.0871	−0.0250	0.0234	−0.0016	−7.84
H(9)−O(10)	1.852	3.380×10^{-2}	0.0947	−0.0268	0.0252	−0.0016	−8.41
O(11)−H(12)	1.907	3.039×10^{-2}	0.0826	−0.0241	0.0234	−0.0017	−7.55
O(13)−H(14)	1.914	2.982×10^{-2}	0.0809	−0.0249	0.0219	−0.0016	−7.38
H(15)−O(16)	1.925	2.913×10^{-2}	0.0785	−0.0230	0.0213	−0.0017	−7.21

[a] $H(r_c) = V(r_c) + G(r_c)$. [b] $E = 0.5 \times V(r_c)$ (to see the position of a particular bond within the molecule described in Table 3, look for the bond length indicated along the structure in the corresponding Figures 7 and 8).

to the XAS measurements, ZnO samples prepared in "pure" aqueous solution are more nanostructured and have missing atoms on the surface compared to those prepared in aqueous NaOH solution. Therefore, the results obtained from the X-ray absorption data and the photocatalytic measurement refinements are in acceptable agreement. For improved photocatalytic activity, it should be emphasized that according to the XAS/FESEM results, a more nanostructured ZnO with missing atoms on the surface of the cluster is one of the desirable properties. It seems that these atom vacancies can be considered as active sites for the improved photocatalytic efficiency of ZnO nanostructures. Most likely, the ZnO nanorods obtained in "pure" aqueous solution show the highest photocatalytic activity due to the presence of a larger amount of oxygen vacancies.

The Mechanism of ZnO Particle Formation. The experimental findings supported by the results of DFT were used to predict the formation mechanism of ZnO particles. It is not possible to fully elucidate the formation mechanism responsible for the preferentially oriented crystal growth of the as-synthesized ZnO particles along the *c*-axis into either a hollow or nonhollow hexagonal structure without considering the nucleation processes. It seems most likely that the prenucleation intermediate formation, as well as their reactivity, represents a bottleneck that, in addition to the nucleation processes, determines all other subsequent crystal growth steps and, thus ultimately, the hierarchical growth of ZnO microstructures.

The Nucleation Process. The mechanism of prenucleation intermediate formation was investigated by taking into account the results of quantum chemical calculations using density functional theory (DFT). According to the DFT study, monomeric and other kinds of stable oligomeric $(ZnO-H_2O)_n$ and/or $(ZnO-OH)_n$ $(n \leq 4)$ species can be considered as components of the prenucleation intermediates that initiated the nucleation processes of ZnO NPs in the "pure" aqueous solution and the NaOH aqueous solution, respectively. The DFT calculations revealed all possible binding interactions involved in the processes of nucleation and growth of ZnO nanosubstructures and microstructures in the presence or absence of NaOH in aqueous media. Of interest is the spontaneous deprotonation reaction of H_2O molecules observed in the most stable monomeric $ZnO-H_2O$ structure due to the high affinity of H_2O molecules for ZnO. As a result of this process of transfer of hydrogen atoms from a H_2O molecule to oxygen on ZnO, the rather high free energy of molecular interaction was released ($\Delta G^*_{INT} = -37.36$ kcal mol^{-1} in $ZnO-H_2O$). In parallel, a free electron pair on the oxygen atom of the water molecule was involved in a new strong coordinate bond with zinc (Zn−O; $E_{Zn-O} = -41.95$ kcal mol^{-1}, $d_{Zn-O} = 1.914$ Å; see Figure 7a).

As is well known from the literature, there are two idealized extremes of chemical bonding: (a) ionic bonding, in which one or more electrons are completely transferred from one atom to another, and (b) covalent bonding, in which the electrons are equally divided between two atoms. However, most compounds have polar covalent bonds, which are intermediate between the two extremes: The bond electrons are unequally distributed between the two atoms, and the electron distribution is asymmetric, with a greater electron density around the more electronegative atom. The polarity of a bond—the extent to which it is polar—is largely determined by the relative electronegativities of the bonded atoms. Thus, there is a direct relationship between the electronegativity and the polarity of a bond. A bond is nonpolar if the bonded atoms have the same electronegativity. However, if the electronegativity of the bonded atoms is not the same, the bond is polarized toward the more electronegative atom. The polarity of the bond and the ionic character increase with increasing differences in electronegativity. In the ZnO bond, the electronegativity of zinc is 1.65 and the electronegativity of oxygen is 3.44, resulting in an electronegativity difference of 1.79. Thus, the bond is characterized by an electronegativity difference between 0 and 2, which is a feature of polar covalent bonds.

In the framework of the quantum theory of atoms in molecules, the critical point of the Zn−O bond was characterized by $\nabla^2\rho(r_c) > 0$ and $H(r_c) < 0$; therefore, the Zn−O bond is attributed to an intermediate type of interaction, as shown in Table 3. The nature of the chemical bond can be described qualitatively by considering the signs and values of the Laplacian of the electron density $\nabla^2\rho(r_c)$ and the electron energy density $H(r_c)$ at the corresponding critical point of the bond according to the following criteria. The interactions characterized by $\nabla^2\rho(r_c) < 0$ and $H(r_c) < 0$ indicate a common interaction, i.e., weakly polar and nonpolar covalent bonds. On the other hand, the interactions denoted by $\nabla^2\rho(r_c) > 0$ and $H(r_c) > 0$ indicate closed-shell interactions such as weak hydrogen bonds, van der Waals interactions, and ionic bonds. Intermediate interactions, which include strong hydrogen bonds and most coordinate bonds, were characterized by $\nabla^2\rho(r_c) > 0$ and $H(r_c) < 0$. A particularly high negative value of $\nabla^2\rho(r_c)$ indicates a strong covalent bond, whereas a high positive value corresponds to a strong noncovalent bond.

https://doi.org/10.1021/acs.inorgchem.1c03905
Inorg. Chem. 2022, 61, 2962−2979

Considering the deprotonation reaction of the H_2O molecules and the transfer of the hydrogen atom to the oxygen of ZnO, as well as the bonding via a new Zn−O coordinate bond, one could conclude that the stability of the system was significantly increased, leading to the particularly stable monomeric ZnO−H_2O species, which are responsible for a very high nucleation rate of the ZnO nuclei. Consequently, the higher concentration of initial nuclei obtained in "pure" aqueous media probably leads to smaller ZnO nanostructures. Moreover, the formation of the most stable $(ZnO-H_2O)_2$ dimer (Figure 7b) with $\Delta G^*_{INT} = -7.76$ kcal mol^{-1} from the association of the most stable ZnO−H_2O monomers with $\Delta G^*_{INT} = -37.36$ kcal mol^{-1} indicates the species for which the association process is less favorable. Interestingly, the calculated Gibbs free energies for the molecular association of ZnO−H_2O revealed a more spontaneous formation of the $(ZnO-H_2O)_4$ tetramer ($\Delta G^*_{INT} = -13.27$ kcal mol^{-1}) (Figure 7c) compared to the $(ZnO-H_2O)_2$ dimer ($\Delta G^*_{INT} = -7.76$ kcal mol^{-1}). The importance of determining the reactivity of ZnO in most applications stems from its interaction with an aqueous medium. However, a thorough understanding of the interaction of ZnO with H_2O at the atomic level is still lacking. A detailed DFT analysis provides mechanistic insights into the reactivity of ZnO NPs that triggers the spontaneous dissociation of H_2O molecules. The Zn and O atoms on the surface have inhomogeneous electronic and geometric topological properties, providing nonequivalent sites for dissociative and molecular H_2O adsorption. The dissociation of H_2O molecules, which is crucial for the formation of reactive O species, has been shown to occur spontaneously at certain Zn surface sites that are electronically modified by the "reactive" O atoms of the surface.[17] Using DFT calculations, the authors have described an atomically detailed mechanism of the reactivity of ZnO NPs with diameters ranging from 9 to 15 Å. This study highlights the importance of spontaneous dissociation of H_2O on the ZnO surface, which is responsible for the reactivity of the NPs and enables the better catalytic activity of the ZnO NPs compared to the macroscopic ZnO surface, which prevents the spontaneous dissociation of a single H_2O. It is possible that the specific atomic surface structures with missing surface atoms offered by the nanostructured ZnO obtained by the hydrothermal synthesis route in "pure" aqueous media are responsible for an enhanced photocatalytic activity compared to those obtained in aqueous NaOH solution. Therefore, the very consistent results of a joint XAS/photocatalysis study are in agreement with the results obtained by DFT.

Namely, when an aqueous NaOH solution was used as a medium instead of "pure" water, ZnO is directly attacked with the free hydroxyl group, and the formation of another (ZnO−OH) species should be emphasized. When the mentioned Zn−O coordinate bond was formed in the (ZnO−OH) species ($E_{Zn-O} = -40.61$ kcal mol^{-1}, $d_{Zn-O} = 1.923$ Å; see Figure 7d), the free energy of molecular interaction was released, $\Delta G^*_{INT} = -18.04$ kcal mol^{-1}. The calculated values of the Gibbs free energy interaction suggest that the set of the particularly stable (ZnO−H_2O) species described above, with $\Delta G^*_{INT} = -37.36$ kcal mol^{-1}, was found to be the main control parameter that triggered the nucleation processes of ZnO NPs in "pure" aqueous media, being twice as stable as the other existing (ZnO−OH) species in aqueous NaOH solution, with $\Delta G^*_{INT} = -18.04$ kcal mol^{-1}. However, the association of the $(ZnO-OH)_2$ dimers increased the stability of the system and led to a particularly stable tetrameric $(ZnO-OH)_4$ species (Figure 7f) with $\Delta G^*_{INT} = -27.14$ kcal mol^{-1}, which is even 9.05 kcal mol^{-1} more stable than the existing $(ZnO-OH)_2$ dimer (Figure 7e) and 9.01 kcal mol^{-1} more stable than the (ZnO−OH) monomer. The more or less spontaneous formation of the most stable $(ZnO-H_2O)_n$ and/or $(ZnO-OH)_n$ ($n \leq 4$) prenucleation intermediates in the "pure" aqueous or aqueous NaOH solution plays a crucial role in the nucleation processes as a key step, which then determines the ZnO crystal growth. The mechanism to control the growth of ZnO nanostructures, which was achieved by manipulating the solution chemistry through the initial addition of NaOH to the aqueous solution, most likely indicates the formation of different nucleation layers. It seems that the two species $(ZnO-OH)_n$ and $(ZnO-H_2O)_n$ described above may have competed with each other and initiated an association process of the nuclei into "cluster nuclei" and the formation of different nucleation layers in aqueous NaOH solution. Thanks mainly to these distinct dynamic processes, these ZnO nuclei tend to aggregate together. In addition, especially the process of tetramerization of a (ZnO−OH) species, favored in aqueous NaOH solution, seems to be considered as the main favorable process for the aggregation of the nuclei into "cluster nuclei". The formation of "cluster nuclei" and the preferential crystal growth actually represent a dynamic equilibrium between the media-dependent processes of interstage formation mentioned above, the growth rate of cluster nuclei, and the dissolution process as assumed in aqueous NaOH solution.

In particular, it is important to emphasize that the direct access of the hydroxyl group from NaOH to ZnO leads to a more spontaneous formation of prenucleation intermediates such as $(ZnO-OH)_2$ dimers ($\Delta G^*_{INT} = -18.09$ kcal mol^{-1}) and even the most stable $(ZnO-OH)_4$ tetramers ($\Delta G^*_{INT} = -27.14$ kcal mol^{-1}), which are almost more than twice as stable compared to the formation of the dimer $(ZnO-H_2O)_2$ ($\Delta G^*_{INT} = -7.76$ kcal mol^{-1}) and tetramer $(ZnO-H_2O)_4$ ($\Delta G^*_{INT} = -13.27$ kcal mol^{-1}) (Table S3). Thus, the calculated Gibbs free energies for the association of the two dimers in aqueous NaOH solution indicate that the amount of these particularly dominant $(ZnO-OH)_4$ tetramers with $\Delta G^*_{INT} = -27.14$ kcal mol^{-1} points to a species that plays a crucial role in the formation processes of the ZnO "cluster cores" among all of them.

However, irrespective of the presence of a hydroxide or water molecule in the appropriate simulated model species, the formation of a fairly similar structural motif with subtle differences is observed for all the dimeric and tetrameric prenucleation species described above, as shown in Figure 7. Due to the high chelating effect of both the water molecule and the hydroxyl group toward zinc, the same tetrahedral geometry has been established in the above species, which increases the stability of zinc. It is important to emphasize that the formation of the structural motif in all the above dimers and tetramers was achieved by a new Zn−O coordinate bond via a free electron pair donation from the oxygen atom to the zinc atoms. Taking into account all the above DFT results, one could conclude that the nucleation process in "pure" aqueous media is mainly carried out by the most stable (ZnO−H_2O) monomers ($\Delta G^*_{INT} = -37.36$ kcal mol^{-1}), while the $(ZnO-OH)_4$ tetramers ($\Delta G^*_{INT} = -27.14$ kcal mol^{-1}) are the most spontaneous among all precursor species in aqueous NaOH solution and play a crucial role in the nucleation

https://doi.org/10.1021/acs.inorgchem.1c03905
Inorg. Chem. 2022, 61, 2962−2979

processes achieved by "cluster nuclei". In summary, when "pure" water is used as the reaction medium, tiny nuclei are formed in a high supersaturation, leading to smaller ZnO nanostructures, while when the medium is changed from aqueous to aqueous NaOH solution, an association of the tiny nuclei into "cluster nuclei" leads to the appearance of larger ZnO nanostructures. Indeed, the aggregation of the nuclei into "cluster nuclei" leads to slowing down of the initial uncontrolled nucleation, which actually means that the nucleation rate is better controlled than in "pure" aqueous solution. Thus, the initial formation of "cluster nuclei" was promoted in the aqueous NaOH solution, which leads to a decrease in the total amount of initial crystalline nuclei of ZnO. Consequently, the lower amount of initial crystalline nuclei is a bottleneck for ZnO growth and leads to a larger ZnO nanostructure in aqueous NaOH solution. Obviously, it is very likely that small ZnO crystallites formed from "cluster cores" have more free spaces to grow, which may lead to the formation of larger ZnO nanosubstructures that are beneficial for further hierarchical crystal growth of hollow spindle-shaped ZnO microstructures with lamellar hexagonal stacks.

The Growth Process. The above results indicate the differences in nucleation processes in "pure" aqueous or aqueous NaOH solution, which consequently determine the two following growth processes, primary ZnO nanosubstructures and potential hierarchical microstructures. However, a more detailed theoretical study is still needed to propose possible growth mechanisms of the primary nanostructures as well as the final hollow hierarchical ZnO microstructures. Therefore, the theoretical study was extended to the construction of other higher oligomeric species to model the possible bonding interactions involved in the processes of ZnO growth and to fully elucidate the growth of hierarchical ZnO microstructures in different reaction media. There is a possibility that the more or less spontaneous formation of other types of stable oligomers (i.e., $(ZnO{-}H_2O)_{12}$ and/or $(ZnO{-}OH)_{12}$ dodecamers) in the "pure" aqueous or aqueous NaOH solution could be responsible for a different growth mechanism of the ZnO nanosubstructures as well as the final microstructures.

In this context, it is important to emphasize the importance of the O−H···O hydrogen bonds, which are the only ones that occur in the formation of the most stable octamers (Table 3) from the association of the two most stable tetramers, as well as the dodecamers (Figure 8) from the association of three tetramers.

Indeed, the DFT calculations revealed shorter H−O distances in the corresponding structural motif in $(ZnO{-}H_2O)_{12}$ ($d_{O\cdots H}$ values from 1.703 to 1.780 Å) compared to $(ZnO{-}OH)_{12}$ ($d_{O\cdots H}$ values from 1.852 to 1.925 Å), highlighting the importance of the differences in the O−H···O hydrogen bonding interaction, which are the only ones occurring upon association of the most stable $(ZnO{-}H_2O)_4$ or $(ZnO{-}OH)_4$ tetramers. Consequently, the calculated values of the energies of a hydrogen bond ($E_{O\cdots H}$ values up to −11.73 kcal mol^{-1}) of the $(ZnO{-}H_2O)_{12}$ interaction indicate stronger bonding in "pure" aqueous solution compared to the interaction of $(ZnO{-}OH)_{12}$ ($E_{O\cdots H}$ values up to −8.41 kcal mol^{-1}) found in the aqueous NaOH solution. The presence of somewhat stronger O−H···O hydrogen bonds in "pure" aqueous media leads to more spontaneous formation of oligomeric species such as octamers and dodecamers, which are related to those that are shaped in aqueous NaOH solution.

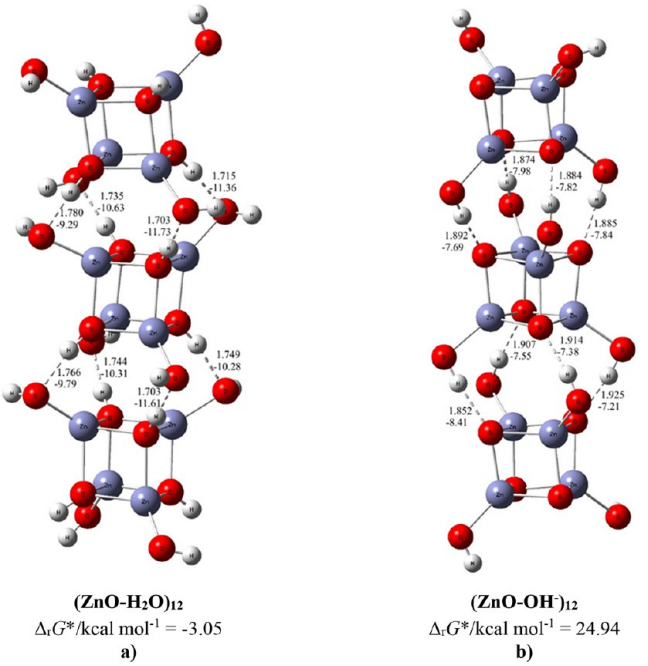

Figure 8. Most stable structures of the $(ZnO{-}H_2O)_{12}$ and $(ZnO{-}OH^-)_{12}$ dodecamers (the bond distances are in Å, and the bond energies are in kcal mol^{-1}).

Such a conclusion follows in particular from the values of the calculated Gibbs free energies of the interactions obtained for $(ZnO{-}H_2O)_{12}$ compared to $(ZnO{-}OH)_{12}$. Indeed, it is important to emphasize that the formation of the most stable octamers and dodecamers occurs only in the "pure" aqueous medium as a spontaneous exergonic process with ΔG^*_{INT} = −1.04 kcal mol^{-1} for $(ZnO{-}H_2O)_8$ but even more so for $(ZnO{-}H_2O)_{12}$ with ΔG^*_{INT} = −3.05 kcal mol^{-1}, while it is endergonic in aqueous NaOH solution ($\Delta G^*_{INT} > 0$) (Figure 8 and Figure S3). In other words, in the presence of aqueous NaOH solution as the reaction medium, the formation of the most stable $(ZnO{-}OH)_8$ octamer (Figure S3) with ΔG^*_{INT} = 17.07 kcal mol^{-1} and the most stable $(ZnO{-}OH)_{12}$ dodecamer with ΔG^*_{INT} = 24.94 kcal mol^{-1} indicates a species for which the association of the most stable tetramers is a rather unfavorable endergonic process. The tendency to form a rather similar structural motif in all the oligomeric species described above is established by the DFT study, as shown in Figure 8 and Figure S3. It is important to emphasize that in the formation of both octamers and dodecamers, the association of $(ZnO{-}H_2O)_4$ and $(ZnO{-}OH)_4$ tetramers occurred via four O−H···O hydrogen bonds. Of particular note are the advantages of the association of a $(ZnO{-}H_2O)_4$ tetramer in the formation of a $(ZnO{-}H_2O)_{12}$ dodecamer with ΔG^*_{INT} = −3.05 kcal mol^{-1} compared to the association of a $(ZnO{-}OH)_4$ tetramer to a $(ZnO{-}OH)_{12}$ dodecamer with ΔG^*_{INT} = 24.94 kcal mol^{-1}, which is more stable by 27.99 kcal mol^{-1} due to the presence of much stronger O−H···O hydrogen bonds. It seems that the spontaneous exorgenic formation process ($\Delta G^*_{INT} < 0$) of the most stable octamers and dodecamers achieved in "pure" aqueous media, as well as the endorgenic formation process ($\Delta G^*_{INT} > 0$) in aqueous NaOH solution, determines the preferential growth process of ZnO nanostructures. The DFT results, both the calculated values of the energies, of the Gibbs free energies of the interactions and of the hydrogen bonds, and in particular the specific structural

https://doi.org/10.1021/acs.inorgchem.1c03905
Inorg. Chem. 2022, 61, 2962−2979

motif of the dodecamers shown in Figure 8, provide evidence that the formation of anisotropic nanocrystalline ZnO with the *c*-axis as the primary growth direction is significantly accelerated in "pure" aqueous reaction media and is very sensitive to the addition of NaOH, as shown by the PXRD results confirming the preferential growth changes in the crystallite regions (Figure 2). Moreover, the calculated DFT results indicate a rather complex nature of the formation and growth mechanism of ZnO nanosubstructures and then microstructures, which can be thermodynamically considered as a sequence of thermodynamic barriers, including the energy for the formation of prenucleation intermediates, that initiate nucleation and preferential nanocrystalline growth, as well as their hierarchical growth by stacking nanosubstructures. The most stable $(ZnO{-}H_2O)_n$ and $(ZnO{-}OH)_n$ structures ($n \leq 12$) and the calculated values of Gibbs free energies of the interactions are listed in Table S3 and depicted in Figure S3, while the bond lengths (d), energies (E), and QTAIM properties of the selected bonds in monomers, dimers, and oligomers are summarized in Table 3.

The correlation of the results from DFT with the results of PXRD structural analysis is crucial to greatly simplify the interpretation of the preferential growth changes in the crystallite domains. The hexagonal wurtzite ZnO is a typical polar crystal with preferential growth along the [0001] direction. The PXRD analysis of all prepared samples shows the formation of a hexagonal wurtzite ZnO structure, albeit with subtle but clearly discernible differences depending on the reaction medium and other details of the preparation. According to the PXRD measurements, the relative intensities between (100), (002), and (101) Bragg reflections of the ZnO samples prepared in "pure" aqueous solution and aqueous NaOH solution have changed, which can be associated with preferential growth changes in the crystallite domains. Of particular note is the decrease in the observed I_{002}/I_{100} values from 1.10 to 0.33 upon addition of NaOH. The observed results indicate that the growth of ZnO structures oriented along the *c*-axis is clearly preferred in "pure" aqueous solution compared to aqueous NaOH solution. In addition to these preferential growth changes in the crystallite domains, the correlation of the results from DFT with the HRTEM/FESEM (surface morphology imaging) results of the present study allows us to draw a general conclusion regarding the overall shape of the NPs as a function of the subtle preparation conditions. Thus, the specific structural motif of the $(ZnO{-}H_2O)_{12}$ dodecamers visible in the DFT model structure with calculated negative ΔG^*_{INT} release energy (Figure 8a) indicates that the formation of an anisotropic nanocrystalline ZnO with the *c*-axis as the primary growth direction is significantly accelerated in "pure" aqueous reaction media compared to aqueous NaOH solution, resulting in thin ZnO nanorods that preferentially grow in the typical growth direction along the *c*-axis (according to the PXRD/HRTEM/FESEM results, Figures 2−4). As shown in a discussion of the FESEM/HRTEM/PXRD results of the present study and according to DFT calculations, the growth of nanostructures in the directions perpendicular to the *c*-axis was suppressed in "pure" aqueous solution. It seems that the elongation and constriction of ZnO particles in aqueous solution could be explained by the effect of water on the reactivity of individual crystal facets during crystal growth. Numerous experimental and theoretical studies indicate molecular and dissociative adsorption of water molecules on ZnO surfaces.[15,17,61]

Moreover, the nanoscale ZnO substructures have a high tendency to stack into microstructures through the secondary growth process. However, the mechanism of the secondary growth process of ZnO microstructures is quite complicated and involves noncovalent interactions such as hydrogen bonds, electrostatic forces, the screening effect, etc. Obviously, both the preferential ZnO nano- and microstructure growth processes are controlled by O−H···O hydrogen bonds, which allow faster or slower growth along the preferential *c*-axis. In summary, the correlation of the results of both the theoretical and experimental studies indicates a different growth mechanism of the final ZnO microstructures, highlighting the tendency for hierarchical lamellar stacking of the hexagonal nanosubstructures in aqueous NaOH solution compared to lateral stacking of the nanosubstructures in "pure" aqueous media during the preferential crystal growth along the *c*-axis. Namely, in the second phase in the aqueous NaOH solution, giant hollow spindle-shaped particles were obtained, which grew layer by layer with lamellar hexagonal stacks and exhibited a hierarchical microstructure (Figure 3, left panel). On the other hand, primary thin nanorods obtained in "pure" aqueous solution have a high tendency to stack laterally in the second growth phase, resulting in elongated, nonhollow ZnO microstructures (Figure 3e, inset). This is quite different from the presumed mechanism of lamellar hierarchical stacking of hexagonal nanodiscs leading to the formation of spindle-shaped ZnO in aqueous NaOH solution.

The O−H···O bonds described above contribute to the effectiveness of attaching lamellar substructures as well as to the compactness of ZnO microstructures composed of laterally stacked thin nanorods. It appears that the presence of stronger O−H··O-hydrogen bonds in "pure" aqueous media ($E_{O\cdots H}$ values up to −11.73 kcal mol^{-1}) contributes even more to the stability, compactness, and smoothness of ZnO microstructures compared to those in aqueous NaOH solution ($E_{O\cdots H}$ values up to −8.41 kcal mol^{-1}). Moreover, it seems that more significant stability of final ZnO particles was achieved when only water is used as reaction media. On the other side, increasing the concentration of OH^- ions appears to enhance the reactivity at the solid−liquid interface and hence favors the formation of completely hollow hexagonal ZnO microtubes, according to FESEM (see Figure 3c). Namely, the formation of hollow hexagonal ZnO microstructures for longer aging time as well as the concentration of NaOH is probably the consequence of adsorbed OH^- ions on the most reactive polar {0001} facets of ZnO due to positive Zn^+ electrostatic interaction. These three parameters (i.e., the presence of NaOH, concentration of NaOH, and aging time) are reviewed to evaluate their respective roles.

It is generally considered that the overall shape is determined by combination of structurally related internal (intermolecular bonding preferences or dislocations in crystal) and external experimental details, in particular the solvent effect.[62,63] Correlation of all results of the present study, both experimental and theoretical, points to the strong impact of reaction media on the preferential crystal growth changes and the overall shape of ZnO particles. One can conclude that the specific surface atomic structures with missing atoms, offered by ZnO NPs obtained through the hydrothermal synthesis route in "pure" aqueous media compared with those yielded in aqueous NaOH solution, make them a better choice in solar photocatalysis, as more pollutants can be simply adsorbed and a higher rate of degradation can be achieved.

https://doi.org/10.1021/acs.inorgchem.1c03905
Inorg. Chem. 2022, 61, 2962−2979

CONCLUSIONS

This integrated experimental and theoretical approach provides a deeper insight into the growth mechanism and photocatalytic behavior of hierarchical ZnO structures. In this research, by changing the reaction medium from "pure" aqueous to aqueous NaOH solution, we have investigated the subtle but clearly visible differences in the structural, microstructural, and especially photocatalytic performance of ZnO particles. These morphological and structural differences are reflected in significant changes in the photocatalytic activity estimated by the higher and faster degradation of RhB over ZnO samples prepared in "pure" aqueous solution compared to those that are prepared in aqueous NaOH solution. The results obtained from the X-ray absorption data and the refinements of the photocatalytic measurements are in acceptable agreement. It was found that the ZnO samples obtained in "pure" aqueous solution have more nanostructures with missing atoms on the surface compared to those prepared in aqueous NaOH solution. Apparently, these atom vacancies can be considered as active sites for the enhanced photocatalytic efficiency of ZnO nanostructures. The experimental findings, confirmed by the results of DFT, were used to predict the nucleation and crystal growth mechanism of ZnO particles. The calculations indicate that the process of ZnO nucleation in aqueous solution is mainly through the reaction of small monomers, while tetramers play a crucial role in aqueous NaOH solution. In summary, when "pure" water was used as the reaction medium, the tiny nuclei were formed in a high supersaturation, leading to smaller ZnO nanostructures, while when the medium was changed from aqueous to aqueous NaOH solution, an association of tiny nuclei to "cluster nuclei" led to the appearance of larger ZnO nanostructures.

Consequently, the differences in nucleation processes in "pure" aqueous or aqueous NaOH solution determine the two following growth processes, primary ZnO nanosubstructures and potential hierarchical microstructures. The correlation of the results of both the theoretical and experimental studies indicates a different growth mechanism of the ZnO nano- and microstructures, revealing the tendency of hierarchical lamellar stacking of hexagonal nanodiscs in aqueous NaOH solution compared to lateral stacking of nanorods in "pure" aqueous media during the preferential crystal growth along the *c*-axis. Both preferential growth processes of the ZnO nanostructures and microstructures are driven by O−H···O hydrogen bonds as the controlling elements. The calculated values of the $E_{O\cdots H}$ interaction indicate a stronger interaction via O−H···O hydrogen bonds in "pure" aqueous media ($E_{O\cdots H}$ values up to −11.73 kcal mol^{-1}) compared to those obtained in aqueous NaOH solution ($E_{O\cdots H}$ values up to −8.41 kcal mol^{-1}).

A decrease in the observed I_{002}/I_{100} values upon addition of NaOH has provided an indication of the pronounced preferential growth rate of the ZnO structures oriented along the *c*-axis in "pure" aqueous solution compared to aqueous NaOH solution. A synergistic effect between the I_{002}/I_{100} values and the crystallite size on the photocatalytic activity was found. Namely, the increased I_{002}/I_{100} ratio observed in "pure" aqueous media significantly enhanced the photocatalytic activity. It seems that the crystallite size and the I_{002}/I_{100} ratio are primarily related to the photocatalytic activity. The correlation of the DFT results with the PXRD/XAS/HRTEM/FESEM results of the present study allows us to link to the general conclusions regarding the preferential growth changes in the crystallite domains as well as the overall particle shape as a function of the subtle preparation conditions. The specific structural motif of the $(ZnO-H_2O)_{12}$ dodecamers with calculated negative ΔG^*_{INT} release energy indicates that the formation of anisotropic nanocrystalline ZnO with the *c*-axis as the primary growth direction is spontaneous and accelerated in "pure" aqueous media, while it is an unfavorable endergonic process in aqueous NaOH solution ($\Delta G^*_{INT} > 0$). The advantages of $(ZnO-H_2O)_4$ tetramer association in the formation of $(ZnO-H_2O)_{12}$ dodecamers ($\Delta G^*_{INT} = -3.05$ kcal mol^{-1}) in "pure" aqueous solution should be emphasized in comparison with the association of $(ZnO-OH)_4$ tetramers to $(ZnO-OH)_{12}$ dodecamers in aqueous NaOH solution. It seems that the spontaneous exorgenic formation process ($\Delta G^*_{INT} < 0$) of the most stable dodecamers achieved in "pure" aqueous media, as well as the endorgenic formation process ($\Delta G^*_{INT} > 0$) in aqueous NaOH solution, determines the preferential growth process of ZnO nanostructures.

It can be concluded that increasing the concentration of OH^- ions seems to increase the reactivity at the solid−liquid interface, thus favoring the formation of fully hollow hexagonal ZnO microtubes, according to FESEM micrographs. In particular, the presence of much stronger O−H···O hydrogen bonds in "pure" aqueous media contributes even more to the stability and compactness as well as smooth facets of the ZnO particles than in aqueous NaOH solution.

ASSOCIATED CONTENT

Supporting Information

The Supporting Information is available free of charge at https://pubs.acs.org/doi/10.1021/acs.inorgchem.1c03905.

Table with unit cell metrics extracted from the Rietveld refinements, details of the computational methods, UV−vis absorption spectra of the RhB solution as a function of illumination time, optimized structures of studied species, tables of interaction Gibbs free energies, and table of optimized Cartesian atomic coordinates (PDF)

$ZnO-H_2O$ monomer (XYZ)

$ZnO-H_2O$ dimer (XYZ)

$ZnO-H_2O$ tetramer (XYZ)

$ZnO-H_2O$ octamer (XYZ)

$ZnO-H_2O$ dodecamer (XYZ)

ZnO−OH monomer (XYZ)

ZnO−OH dimer (XYZ)

ZnO−OH tetramer (XYZ)

ZnO−OH octamer (XYZ)

ZnO−OH dodecamer (XYZ)

AUTHOR INFORMATION

Corresponding Author

Ankica Šarić − *Ruđer Bošković Institute, Division of Materials Physics, Centre of Excellence for Advanced Materials and Sensing Devices, HR-10002 Zagreb, Croatia;* orcid.org/0000-0002-3211-2360; Phone: +385 1 45 61 111; Email: Ankica.Saric@irb.hr; Fax: +385 1 46 80 098

Authors

Martina Vrankić − *Ruđer Bošković Institute, Division of Materials Physics, Centre of Excellence for Advanced Materials and Sensing Devices, HR-10002 Zagreb, Croatia*

https://doi.org/10.1021/acs.inorgchem.1c03905
Inorg. Chem. 2022, 61, 2962−2979

Dirk Lützenkirchen-Hecht − *Fk. 4, Physik, Bergische Universität Wuppertal, D-42097 Wuppertal, Germany*
Ines Despotović − *Division of Physical Chemistry, Ruđer Bošković Institute, HR-10002 Zagreb, Croatia*
Željka Petrović − *Division of Materials Chemistry, Ruđer Bošković Institute, HR-10002 Zagreb, Croatia*
Goran Dražić − *Department of Materials Chemistry, National Institute of Chemistry, SI-1001 Ljubljana, Slovenia;* orcid.org/0000-0001-7809-8050
Franz Eckelt − *Fk. 4, Physik, Bergische Universität Wuppertal, D-42097 Wuppertal, Germany*

Complete contact information is available at: https://pubs.acs.org/10.1021/acs.inorgchem.1c03905

Notes

The authors declare no competing financial interest.

■ ACKNOWLEDGMENTS

The authors would like to thank mag. ing. arch. Marin Josipović for the help with graphic expression. We gratefully acknowledge the financial support from the Croatian Academy of Sciences. The authors kindly acknowledge the support from the SAFU (grant KK.01.1.1.01.0001). The authors would like to thank the Zagreb University Computing Centre (SRCE) for generously providing computing resources on the cluster ISABELLA (isabella.srce.hr). G.D. gratefully acknowledges the financial support from the Slovenian Research Agency (P2-0393). The authors would like to thank DELTA for the provision of beamtime and the support of the experiments presented here.

■ REFERENCES

(1) Marcì, G.; Augugliaro, V.; López-Muñoz, M. J.; Martín, C.; Palmisano, L.; Rives, V.; Schiavello, M.; Tilley, R. J. D.; Venezia, A. M. Preparation Characterization and Photocatalytic Activity of Polycrystalline ZnO/TiO_2 Systems. 2. Surface, Bulk Characterization, and 4-Nitrophenol Photodegradation in Liquid−Solid Regime. *J. Phys. Chem. B* **2001**, *105*, 1033−1040.
(2) Singh, S.; Joshi, M.; Panthari, P.; Malhotra, B.; Kharkwal, A. C.; Kharkwal, H. Citrulline Rich Structurally Stable Zinc Oxide Nanostructures for Superior Photo Catalytic and Optoelectronic Applications: A Green Synthesis Approach. *Nanostruct. Nanoobjects* **2017**, *11*, 1−6.
(3) Li, Y.; Zhang, X.; Jiang, S.; Dai, H.; Sun, X.; Li, Y. Improved Photoelectrochemical Property of a Nanocomposite NiO/CdS@ZnO Photoanode for Water Splitting. *Sol. Energy Mater. Sol. Cells* **2015**, *132*, 40−46.
(4) Huang, M.; Yan, Y.; Feng, W.; Weng, S.; Zheng, Z.; Fu, X.; Liu, P. Controllable Tuning Various Ratios of ZnO Polar Facets by Crystal Seed-Assisted Growth and Their Photocatalytic Activity. *Cryst. Growth Des.* **2014**, *14*, 2179−2186.
(5) Zheng, Y.; Chen, C.; Zhan, Y.; Lin, X.; Zheng, Q.; Wei, K.; Zhu, J.; Zhu, Y. Luminescence and Photocatalytic Activity of ZnO Nanocrystals: Correlation between Structure and Property. *Inorg. Chem.* **2007**, *46*, 6675−6682.
(6) Gupta, J.; Barick, K. C.; Bahadur, D. Defect Mediated Photocatalytic Activity in Shape-Controlled ZnO Nanostructures. *J. Alloys Compd.* **2011**, *509*, 6725−6730.
(7) Ong, C. B.; Ng, L. Y.; Mohammad, A. W. A Review of ZnO Nanoparticles as Solar Photocatalysts: Synthesis, Mechanisms and Applications. *Renewable Sustainable Energy Rev.* **2018**, *81*, 536−551.
(8) Narayana, A.; Bhat, S. A.; Fathima, A.; Lokesh, S. V.; Surya, S. G.; Yelamaggad, C. V. Green and Low-Cost Synthesis of Zinc Oxide Nanoparticles and Their Application in Transistor-Based Carbon Monoxide Sensing. *RSC Adv.* **2020**, *10*, 13532−13542.
(9) Montero-Muñoz, M.; Ramos-Ibarra, J. E.; Rodríguez-Páez, J. E.; Marques, G. E.; Teodoro, M. D.; Coaquira, J. A. H. Growth and Formation Mechanism of Shape-Selective Preparation of ZnO Structures: Correlation of Structural, Vibrational and Optical Properties. *Phys. Chem. Chem. Phys.* **2020**, *22*, 7329−7339.
(10) Lim, H.; Yusuf, M.; Song, S.; Park, S.; Park, K. H. Efficient Photocatalytic Degradation of Dyes Using Photo-Deposited Ag Nanoparticles on ZnO Structures: Simple Morphological Control of ZnO. *RSC Adv.* **2021**, *11*, 8709−8717.
(11) Wiesmann, N.; Tremel, W.; Brieger, J. Zinc Oxide Nanoparticles for Therapeutic Purposes in Cancer Medicine. *J. Mater. Chem. B* **2020**, *8*, 4973−4989.
(12) Liu, Y.; He, L.; Mustapha, A.; Li, H.; Hu, Z. Q.; Lin, M. Antibacterial Activities of Zinc Oxide Nanoparticles against Escherichia Coli O157:H7. *J. Appl. Microbiol.* **2009**, *107*, 1193−1201.
(13) Kaushik, N.; Anang, S.; Ganti, K. P.; Surjit, M. Zinc: A Potential Antiviral Against Hepatitis E Virus Infection? *DNA Cell Biol.* **2018**, *37*, 593−599.
(14) Hamdi, M.; Abdel-Bar, H. M.; Elmowafy, E.; El-khouly, A.; Mansour, M.; Awad, G. A. S. Investigating the Internalization and COVID-19 Antiviral Computational Analysis of Optimized Nanoscale Zinc Oxide. *ACS Omega* **2021**, *6*, 6848−6860.
(15) Wang, Y.; Muhler, M.; Wöll, C. Spectroscopic Evidence for the Partial Dissociation of H2O on ZnO(100). *Phys. Chem. Chem. Phys.* **2006**, *8*, 1521−1524.
(16) Raymand, D.; van Duin, A. C. T.; Goddard, W. A.; Hermansson, K.; Spångberg, D. Hydroxylation Structure and Proton Transfer Reactivity at the Zinc Oxide−Water Interface. *J. Phys. Chem. C* **2011**, *115*, 8573−8579.
(17) Rawal, T. B.; Ozcan, A.; Liu, S.-H.; Pingali, S. V.; Akbilgic, O.; Tetard, L.; O'Neill, H.; Santra, S.; Petridis, L. Interaction of Zinc Oxide Nanoparticles with Water: Implications for Catalytic Activity. *ACS Appl. Nano Mater.* **2019**, *2*, 4257−4266.
(18) Wojnarowicz, J.; Chudoba, T.; Koltsov, I.; Gierlotka, S.; Dworakowska, S.; Lojkowski, W. Size Control Mechanism of ZnO Nanoparticles Obtained in Microwave Solvothermal Synthesis. *Nanotechnology* **2018**, *29*, 065601−065623.
(19) Wang, J.; An, X.; Li, Q.; Egerton, R. F. Size-Dependent Electronic Structures of ZnO Nanowires. *Appl. Phys. Lett.* **2005**, *86*, 201911−201913.
(20) Li, C.; Koenigsmann, C.; Ding, W.; Rudshteyn, B.; Yang, K. R.; Regan, K. P.; Konezny, S. J.; Batista, V. S.; Brudvig, G. W.; Schmuttenmaer, C. A.; Kim, J.-H. Facet-Dependent Photoelectrochemical Performance of TiO_2 Nanostructures: An Experimental and Computational Study. *J. Am. Chem. Soc.* **2015**, *137*, 1520−1529.
(21) Chiou, J. W.; Kumar, K. P. K.; Jan, J. C.; Tsai, H. M.; Bao, C. W.; Pong, W. F.; Chien, F. Z.; Tsai, M.-H.; Hong, I.-H.; Klauser, R.; Lee, J. F.; Wu, J. J.; Liu, S. C. Diameter Dependence of the Electronic Structure of ZnO Nanorods Determined by X-Ray Absorption Spectroscopy and Scanning Photoelectron Microscopy. *Appl. Phys. Lett.* **2004**, *85*, 3220−3222.
(22) Erat, S.; Ozkendir, O. M.; Yildirimcan, S.; Gunaydin, S.; Harfouche, M.; Demir, B.; Braun, A. Study on Crystallographic and Electronic Structure of Micrometre-Scale ZnO and ZnO:B Rods via X-Ray Absorption Fine-Structure Spectroscopy. *J. Synchrotron Rad.* **2021**, *28*, 448−454.
(23) Šarić, A.; Štefanić, G.; Dražić, G.; Gotić, M. Solvothermal Synthesis of Zinc Oxide Microspheres. *J. Alloys Compd.* **2015**, *652*, 91−99.
(24) Šarić, A.; Despotović, I.; Štefanić, G.; Dražić, G. The Influence of Ethanolamines on the Solvothermal Synthesis of Zinc Oxide: A Combined Experimental and Theoretical Study. *ChemistrySelect* **2017**, *2*, 10038−10049.
(25) Šarić, A.; Despotović, I.; Štefanić, G. Solvothermal Synthesis of Zinc Oxide Nanoparticles: A Combined Experimental and Theoretical Study. *J. Mol. Struct.* **2019**, *1178*, 251−260.
(26) Šarić, A.; Despotović, I.; Štefanić, G. Alcoholic Solvent Influence on ZnO Synthesis: A Joint Experimental and Theoretical Study. *J. Phys. Chem. C* **2019**, *123*, 29394−29407.

(27) Vrankić, M.; Šarić, A.; Nakagawa, T.; Ding, Y.; Despotović, I.; Kanižaj, L.; Ishii, H.; Hiraoka, N.; Dražić, G.; Lützenkirchen-Hecht, D.; Peter, R.; Petravić, M. Pressure-Induced and Flaring Photocatalytic Diversity of ZnO Particles Hallmarked by Finely Tuned Pathways. *J. Alloys Compd.* **2022**, *894*, 162444.
(28) Wang, F.; Qin, X.; Guo, Z.; Meng, Y.; Yang, L.; Ming, Y. Hydrothermal Synthesis of Dumbbell-Shaped ZnO Microstructures. *Ceram. Int.* **2013**, *39*, 8969−8973.
(29) Musić, S.; Šarić, A. Formation of Hollow ZnO Particles by Simple Hydrolysis of Zinc Acetylacetonate. *Ceram. Int.* **2012**, *38*, 6047−6052.
(30) Anžlovar, A.; Kogej, K.; Orel, Z. C.; Žigon, M. Impact of Inorganic Hydroxides on ZnO Nanoparticle Formation and Morphology. *Cryst. Growth Des.* **2014**, *14*, 4262−4269.
(31) Zhang, Y.; Mu, J. Controllable Synthesis of Flower- and Rod-like ZnO Nanostructures by Simply Tuning the Ratio of Sodium Hydroxide to Zinc Acetate. *Nanotechnology* **2007**, *18*, 075606−075612.
(32) Akir, S.; Barras, A.; Coffinier, Y.; Bououdina, M.; Boukherroub, R.; Omrani, A. D. Eco-Friendly Synthesis of ZnO Nanoparticles with Different Morphologies and Their Visible Light Photocatalytic Performance for the Degradation of Rhodamine B. *Ceram. Int.* **2016**, *42*, 10259−10265.
(33) Huang, M.; Weng, S.; Wang, B.; Hu, J.; Fu, X.; Liu, P. Various Facet Tunable ZnO Crystals by a Scalable Solvothermal Synthesis and Their Facet-Dependent Photocatalytic Activities. *J. Phys. Chem. C* **2014**, *118*, 25434−25440.
(34) Wu, L.; Wu, Y. Synthesis and Optical Characteristic of ZnO Nanorod. *J. Mater. Sci.* **2007**, *42*, 406−408.
(35) Wang, Z.; Qian, X.; Yin, J.; Zhu, Z. Large-Scale Fabrication of Tower-like, Flower-like, and Tube-like ZnO Arrays by a Simple Chemical Solution Route. *Langmuir* **2004**, *20*, 3441−3448.
(36) Chaudhari, R.; Landge, D.; Bhongale, C. J. A New Insight into the Adsorption−Dissolution Growth Mechanism of Zinc Oxide Hollow Hexagonal Nanotowers. *RSC Adv.* **2019**, *9*, 20728−20732.
(37) Yu, Q.; Fu, W.; Yu, C.; Yang, H.; Wei, R.; Li, M.; Liu, S.; Sui, Y.; Liu, Z.; Yuan, M.; Zou, G.; Wang, G.; Shao, C.; Liu, Y. Fabrication and Optical Properties of Large-Scale ZnO Nanotube Bundles via a Simple Solution Route. *J. Phys. Chem. C* **2007**, *111*, 17521−17526.
(38) Wei, A.; Sun, X. W.; Xu, C. X.; Dong, Z. L.; Yang, Y.; Tan, S. T.; Huang, W. Growth Mechanism of Tubular ZnO Formed in Aqueous Solution. *Nanotechnology* **2006**, *17*, 1740−1744.
(39) Zhang, J.; Sun, L.; Liao, C.; Yan, C. A Simple Route towards Tubular ZnO. *Chem. Commun.* **2002**, *3*, 262−263.
(40) Yao, Z.; Postma, H. W. C.; Balents, L.; Dekker, C. Carbon Nanotube Intramolecular Junctions. *Nature* **1999**, *402*, 273−276.
(41) Hu, J. Q.; Bando, Y. Growth and Optical Properties of Single-Crystal Tubular ZnO Whiskers. *Appl. Phys. Lett.* **2003**, *82*, 1401−1403.
(42) Rietveld, H. M. A Profile Refinement Method for Nuclear and Magnetic Structures. *J. Appl. Crystallogr.* **1969**, *2*, 65−71.
(43) Toby, B. H.; Von Dreele, R. B. GSAS-II: The Genesis of a Modern Open-Source All Purpose Crystallography Software Package. *J. Appl. Crystallogr.* **2013**, *46*, 544−549.
(44) Lützenkirchen-Hecht, D.; Wagner, R.; Szillat, S.; Hüsecken, A. K.; Istomin, K.; Pietsch, U.; Frahm, R. The Multi-Purpose Hard X-Ray Beamline BL10 at the DELTA Storage Ring. *J. Synchrotron Rad.* **2014**, *21*, 819−826.
(45) Ravel, B.; Newville, M. ATHENA and ARTEMIS: Interactive Graphical Data Analysis Using IFEFFIT. *Phys. Scr.* **2005**, *2005*, 1007−1010.
(46) Zabinsky, S. I.; Rehr, J. J.; Ankudinov, A.; Albers, R. C.; Eller, M. J. Multiple-Scattering Calculations of x-Ray-Absorption Spectra. *Phys. Rev. B* **1995**, *52*, 2995−3009.
(47) Frisch, M. J.; Trucks, G. W.; Schlegel, H. B.; Scuseria, G. E.; Robb, M. A.; Cheeseman, J. R.; Scalmani, G.; Barone, V.; Mennucci, B.; Petersson, G. A.; Nakatsuji, H.; Caricato, M.; Li, X.; Hratchian, H. P.; Izmaylov, A. F.; Bloino, J.; Zheng, G.; Sonnenberg, J. L.; Hada, M.; Ehara, M.; Toyota, K.; Fukuda, R.; Hasegawa, J.; Ishida, M.; Nakajima, T.; Honda, Y.; Kitao, O.; Nakai, H.; Vreven, T.; Montgomery, J. A., Jr.; Peralta, J. E.; Ogliaro, F.; Bearpark, M.; Heyd, J. J.; Brothers, E.; Kudin, K. N.; Staroverov, V. N.; Kobayashi, R.; Normand, J.; Raghavachari, K.; Rendell, A.; Burant, J. C.; Iyengar, S. S.; Tomasi, J.; Cossi, M.; Rega, N.; Millam, J. M.; Klene, M.; Knox, J. E.; Cross, J. B.; Bakken, V.; Adamo, C.; Jaramillo, J.; Gomperts, R.; Stratmann, R. E.; Yazyev, O.; Austin, A. J.; Cammi, R.; Pomelli, C.; Ochterski, J. W.; Martin, R. L.; Moroku-ma, K.; Zakrzewski, V. G.; Voth, G. A.; Salvador, P.; Dannenberg, J. J.; Dapprich, S.; Daniels, A. D.; Farkas, Ö.; Foresman, J. B.; Ortiz, J. V.; Cioslowski, J.; Fox, D. J. *Gaussian 09*, Revision D.01; Gaussian, Inc.: Wallingford CT, 2009.
(48) Zhao, Y.; Schultz, N. E.; Truhlar, D. G. Design of Density Functionals by Combining the Method of Constraint Satisfaction with Parametrization for Thermochemistry, Thermochemical Kinetics, and Noncovalent Interactions. *J. Chem. Theory Comput.* **2006**, *2*, 364−382.
(49) Hay, P. J.; Wadt, W. R. *Ab Initio* Effective Core Potentials for Molecular Calculations. Potentials for the Transition Metal Atoms Sc to Hg. *J. Chem. Phys.* **1985**, *82*, 270−283.
(50) Marenich, A. V.; Cramer, C. J.; Truhlar, D. G. Universal Solvation Model Based on the Solvent Defined by the Bulk Dielectric Constant and Atomic Surface Tensions. *J. Phys. Chem. B* **2009**, *113*, 6378−6396.
(51) Keith, T. A. *AIMAll (Version 17.01.25)*; TK Gristmill Software: Overland Park KS, USA, 2017.
(52) Bader, R. F. W. *Atoms in Molecules: a Quantum Theory*; Clarendon Press: Oxford, U.K., 1990.
(53) Kisi, E. H.; Elcombe, M. M. U Parameters for the Wurtzite Structure of ZnS and ZnO Using Powder Neutron Diffraction. *Acta Crystallogr., Sect. C: Cryst. Struct. Commun.* **1989**, *45*, 1867−1870.
(54) Nie, D.; Xue, T.; Zhang, Y.; Li, X. Synthesis and Structure Analysis of Aluminum Doped Zinc Oxide Powders. *Sci. Chin. Ser. B Chem.* **2008**, *51*, 823−828.
(55) Vayssieres, L.; Keis, K.; Hagfeldt, A.; Lindquist, S.-E. Three-Dimensional Array of Highly Oriented Crystalline ZnO Microtubes. *Chem. Mater.* **2001**, *13*, 4395−4398.
(56) Kovács, Z.; Molnár, C.; Štangar, U. L.; Cristea, V.-M.; Pap, Z.; Hernadi, K.; Baia, L. Optimization Method of the Solvothermal Parameters Using Box−Behnken Experimental Design—The Case Study of ZnO Structural and Catalytic Tailoring. *Nanomaterials* **2021**, *11*, 1334−1354.
(57) Trandafilović, L. V.; Jovanović, D. J.; Zhang, X.; Ptasińska, S.; Dramićanin, M. D. Enhanced Photocatalytic Degradation of Methylene Blue and Methyl Orange by ZnO:Eu Nanoparticles. *Appl. Catal., B* **2017**, *203*, 740−752.
(58) Liu, X.; Ye, L.; Liu, S.; Li, Y.; Ji, X. Photocatalytic Reduction of CO 2 by ZnO Micro/Nanomaterials with Different Morphologies and Ratios of {0001} Facets. *Sci. Rep.* **2016**, *6*, 38474−38483.
(59) Boppella, R.; Anjaneyulu, K.; Basak, P.; Manorama, S. V. Facile Synthesis of Face Oriented ZnO Crystals: Tunable Polar Facets and Shape Induced Enhanced Photocatalytic Performance. *J. Phys. Chem. C* **2013**, *117*, 4597−4605.
(60) Ravel, B. Quantitative EXAFS Analysis. In *X-Ray Absorption and X-Ray Emission Spectroscopy: Theory and Applications*; VanBokhoven, J. A.; Lamberti, C. Eds., John Wiley & Sons, 2016.
(61) Calzolari, A.; Catellani, A. Water Adsorption on Nonpolar ZnO($10\bar{1}0$) Surface: A Microscopic Understanding. *J. Phys. Chem. C* **2009**, *113*, 2896−2902.
(62) Cheng, B.; Samulski, E. T. Hydrothermal Synthesis of One-Dimensional ZnO Nanostructures with Different Aspect Ratios. *Chem. Commun.* **2004**, *8*, 986−987.
(63) Cheng, B.; Shi, W.; Russell-Tanner, J. M.; Zhang, L.; Samulski, E. T. Synthesis of Variable-Aspect-Ratio, Single-Crystalline ZnO Nanostructures. *Inorg. Chem.* **2006**, *45*, 1208−1214.

https://doi.org/10.1021/acs.inorgchem.1c03905
Inorg. Chem. 2022, 61, 2962−2979